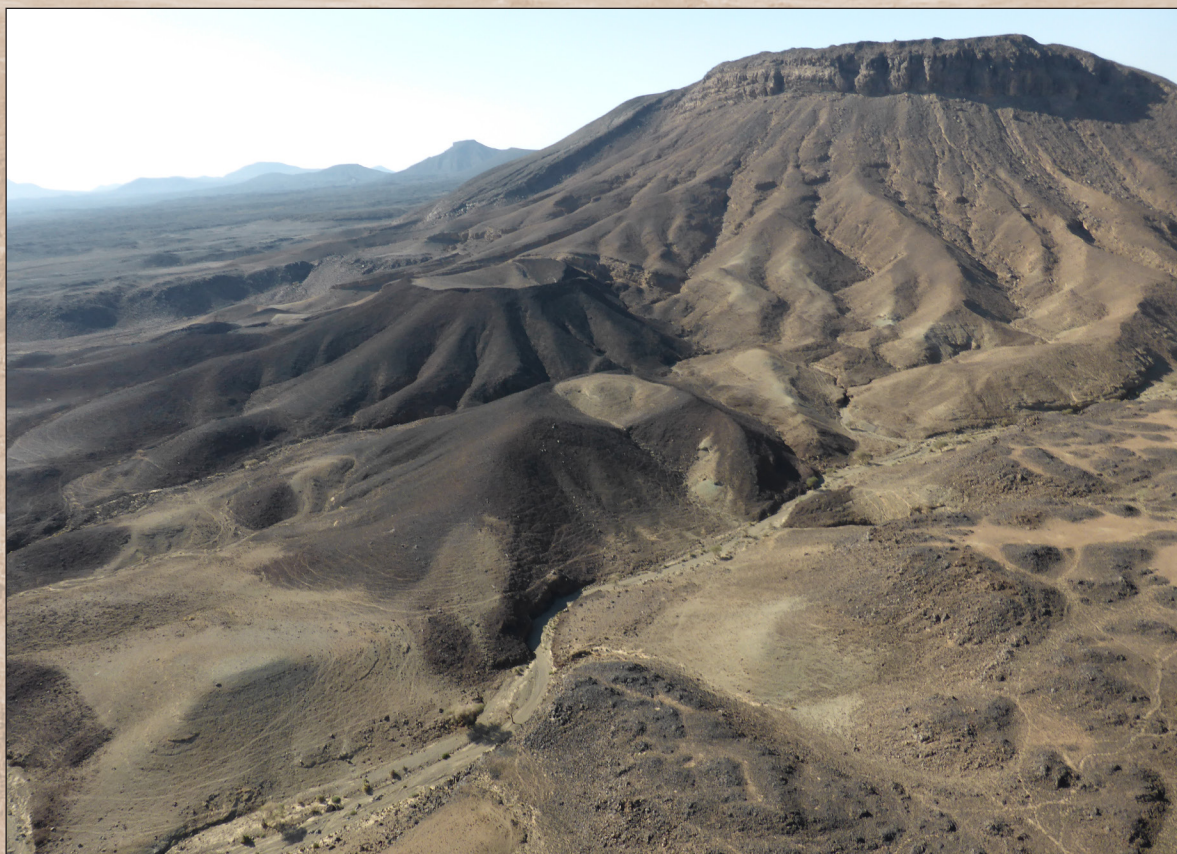# Ground-Motion Prediction Equations for the Western Kingdom of Saudi Arabia

Chapter O of
Active Volcanism on the Arabian Shield—Geology, Volcanology, and Geophysics of Northern Harrat Rahat and Vicinity, Kingdom of Saudi Arabia

U.S. Geological Survey Professional Paper 1862
Saudi Geological Survey Special Report SGS–SP–2021–1

U.S. Department of the Interior
U.S. Geological Survey

Cover. Photograph looking south of the imposing benmoreite of Um Junb which overlaps two scoria cones and associated lava flows of the basalt of Dabaa 1 (foreground). Flat-topped edifice in center distance is the benmoreite of Al Shathaa, several trachyte domes in the Al Efairia volcanic center, and the Holocene trachyte of Um Rgaibah on the left edge of the photograph. U.S. Geological Survey photograph by Andrew Calvert, February 12, 2014. Background image shows northern Harrat Rahat lava flows, maars, and lava domes. U.S. Geological Survey photograph by Andrew Calvert, January 25, 2012.

Ground-Motion Prediction Equations for the Western Kingdom of Saudi Arabia

By Ryota Kiuchi, Walter D. Mooney, and Hani M. Zahran

Chapter O of
Active Volcanism on the Arabian Shield—Geology, Volcanology, and Geophysics of Northern Harrat Rahat and Vicinity, Kingdom of Saudi Arabia

Edited by Thomas W. Sisson, Andrew T. Calvert, and Walter D. Mooney

U.S. Department of the Interior
U.S. Geological Survey

U.S. Geological Survey, Reston, Virginia: 2023

Contents

Figures

Table

Conversion Factors

International System of Units to U.S. customary units

Multiply	By	To obtain
Length		
centimeter (cm)	0.3937	inch (in.)
meter (m)	3.281	foot (ft)
kilometer (km)	0.6214	mile (mi)
meter (m)	1.094	yard (yd)

Datum

Horizontal coordinate information is referenced to the North American Datum of 1983 (NAD 83).

Abbreviations

A10	GMPEs of Atkinson (2010)
BSSA14	GMPEs of Boore and others (2014)
C.E.	Common Era
g	acceleration due to gravity
GMPE	ground-motion prediction equation
H/V	horizontal-to-vertical
Hz	hertz
InSAR	interferometric synthetic aperture radar
M	magnitude
M_L	local magnitude
M_s	surface-wave magnitude
M_w	moment magnitude
NGA	Next Generation Attenuation
PGA	peak ground acceleration
PGV	peak ground velocity
PP04	GMPEs of Pankow and Pechmann (2004)
PSHA	probabilistic seismic hazard analysis
R_{JB}	Joyner-Boore distance
SEA99	GMPEs of Spudich and others (1999)
SGS	Saudi Geological Survey
SNR	signal-to-noise ratio
SNSN	Saudi National Seismic Network
USGS	U.S. Geological Survey
V_{S30}	time averaged shear-wave velocity of the top 30 meters of depth

Chapter O

Ground-Motion Prediction Equations for the Western Kingdom of Saudi Arabia

By Ryota Kiuchi,[1,2] Walter D. Mooney,[1] and Hani M. Zahran[3]

Abstract

Ground-motion prediction equations (GMPEs) for the western Kingdom of Saudi Arabia are developed by employing a mixed-effects regression model to modify the Boore and others (2014) Next Generation Attenuation-West2 (NGA-West2) project GMPEs. NGA-West2 addressed several key issues concerning GMPEs for shallow crustal earthquakes in active tectonic regions. However, the NGA-West2 input data do not include many earthquakes in extensional regimes, such as those occurring in Saudi Arabia. This deficiency is redressed by calculating a magnitude scaling of the new Saudi Arabia-specific GMPEs compared to those of Boore and others (2014). Furthermore, there is a clear difference in distance scaling for the Saudi Arabian GMPEs in comparison with the NGA-West2 GMPEs. This difference is especially significant at large distances and is mainly due to lower anelastic attenuation in the crystalline crust of western Saudi Arabia. Our empirical data demonstrate that the GMPEs presented here are in good agreement with observed earthquake ground motions in western Saudi Arabia.

Introduction

An important requirement for seismic hazard assessment is the development of empirical models for estimating earthquake-generated ground shaking, referred to as ground-motion prediction equations (GMPEs). Such equations are useful for engineering and real-life applications such as seismic design codes and earthquake loss and risk estimation. GMPEs specify the mean and uncertainty of predicted ground motions, in particular peak ground acceleration (PGA) and peak ground velocity (PGV), as a function of magnitude, source-to-site distance, and local site conditions. Many kinds of GMPEs have been developed from distinct or partly overlapping regional datasets, which sometimes causes significant differences in

predicted ground motion for the same scenario earthquake (Bradley, 2013). Specifically, the Next Generation Attenuation-West1 (NGA-West1) project (Power and others, 2008) and the upgraded NGA-West2 project (Bozorgnia and others, 2014) developed GMPEs for shallow crustal earthquakes using a worldwide dataset of seismic recordings. However, the applicability of the NGA-West2 GMPEs for probabilistic seismic hazard analysis (PSHA) is questionable for regions not included in the development of the NGA models. A useful approach to developing local, unique GMPEs has been documented by recent studies in Italy (Scasserra and others, 2009), Hawai'i (Atkinson, 2010), Iran (Shoja-Taheri and others, 2010), New Zealand (Bradley, 2013), and Turkey (Gülerce and others, 2016). These studies developed GMPEs based on regional adjustment factors derived from the differences between ground motions observed in the target regions and those predicted by the NGA GMPEs. As mentioned in Scasserra and others (2009), one of the advantages of this procedure is the use of the functional forms for magnitude and distance scaling of the NGA expressions that were derived from large databases comprising multiple regional datasets. This approach is invaluable in developing more stable regional GMPEs for regions with few recordings.

In the Middle East, Zahran and others (2015, 2016) presented PSHAs for the western Kingdom of Saudi Arabia that were developed using published GMPEs from areas outside of Saudi Arabia (for example, Pankow and Pechmann, 2004; Atkinson and Boore, 2006; Zhao and others, 2006; Akkar and others, 2014). The PSHAs developed by Zahran and others (2015, 2016) were produced by taking the average of those non-Saudi Arabian GMPEs using specific weights for different regions. However, developing region-specific GMPEs for Saudi Arabia that reflect the local earthquake source characteristics, path effects, and geologic setting are needed for more precise estimates of PSHA. Until now, no such region-specific GMPEs for Saudi Arabia have been available, which makes their development an important contribution to future seismic assessment in Saudi Arabia.

Saudi Arabia is surrounded by several active tectonic regions, including extension in the Red Sea and left-lateral

---

[1]U.S. Geological Survey.

[2]Kyoto University.

[3]Saudi Geological Survey.

strike-slip motion in the Gulf of Aqaba and along the Aqaba-Dead Sea Transform boundary (Nehlig and others, 2002). The Aqaba-Dead Sea Transform boundary is an approximately 1,200-kilometer (km)-long fault system that connects the Red Sea with the Zagros fold-thrust belt (fig. 1*A*; Hofstetter and others, 2014). Saudi Arabia has experienced large earthquakes in the past, as is known from both the historical (Ambraseys and others, 2005) and instrumental record (Youssef, 2015; Zahran and others, 2015, 2016). Most earthquakes affecting Saudi Arabia initiate within or near the Red Sea or the Gulf of Aqaba, southern Dead Sea (fig. 1*A*), where a destructive magnitude (*M*) 7.3 event occurred in 1995. In addition, the historical record documents more moderate earthquakes (estimated *M*6–7), such as the 1068 C.E. *M*7 earthquake in the northwestern Arabian Peninsula (Ambraseys and others, 2005). In this area, multiple seismic swarms in and around volcanic fields, also known as harrats, have been detected over the past several decades (El-Isa and Al Shanti, 1989; Pallister and others, 2010). These swarms are thought to be related to regional tectonic stresses that are attributed to rifting in the Red Sea, strike-slip motion along the Aqaba-Dead Sea Transform boundary, and magmatic intrusions (Pallister and others, 2010; Hansen and others, 2013). The most recent large earthquake swarm in the region, which included more than 30,000 earthquakes, occurred from April to June 2009 beneath the volcanic field of Harrat Lunayyir in northwestern Saudi Arabia (fig. 1*B*). The strongest seismic activity occurred May 13–19, 2009, and consisted of events with *M* > 4. The largest earthquake occurred on May 19; its local magnitude (M_L) was 5.4, as estimated by the Saudi Geological Survey (SGS), and its moment magnitude (M_w) was 5.7, according to the U.S. Geological Survey (USGS). The Saudi Arabian Government evacuated 40,000 people from the region in order to avoid casualties from a possible aftershock. Analysis of the M_w 5.7 earthquake using interferometric synthetic aperture radar (InSAR) data concluded that it was associated with intrusion of a shallow magmatic dike (Pallister and others, 2010; Baer and Hamiel, 2010).

In this study, we developed new GMPEs for western Saudi Arabia with local earthquake data from the SGS by modifying the GMPEs of Boore and others (2014) (referred to as BSSA14). Our main goal for developing these new GMPEs is to improve the accuracy of seismic hazard analyses for Saudi Arabia presented by Zahran and others (2015, 2016). Since PGA and PGV values are the basic parameters for such analysis, we focus on these ground motions. In the following sections we first describe the BSSA14 reference GMPEs. Then, our dataset is described. Subsequently, the observed recordings are compared with the BSSA14 model. The BSSA14 model is then modified to create western Saudi Arabia-specific GMPEs that account for the differences in the seismic records in Saudi Arabia as compared to the BSSA14 predictions. Finally, we consider a modest extrapolation of the magnitude range of our Saudi Arabian GMPEs in view of the more limited magnitude range of the observed earthquake recordings. We also discuss the difference in the anelastic attenuation between the BSSA14 and Saudi Arabian GMPEs in terms of the contrasting tectonic settings for these GMPEs.
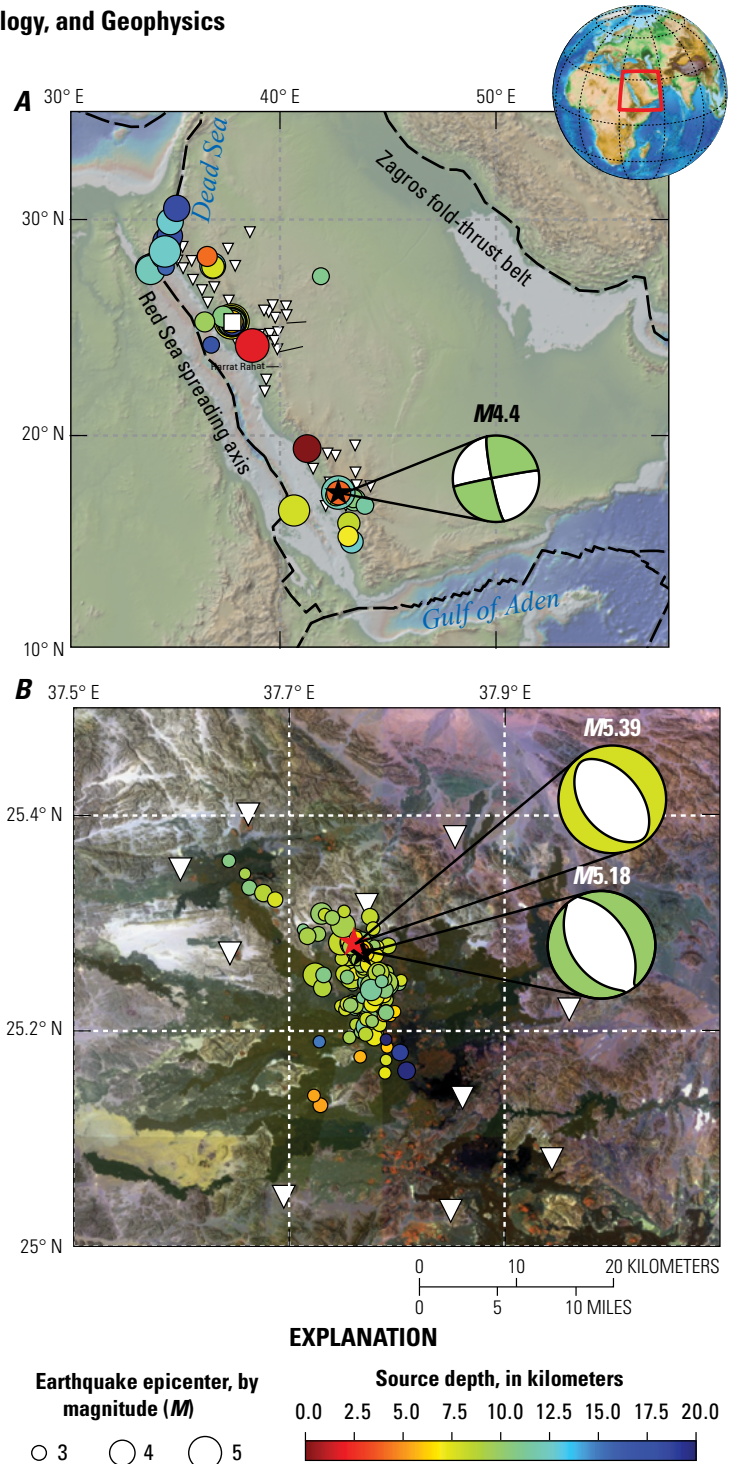
Figure 1. *A*, Map showing the distribution of events used in this study with colors representing source depth as estimated in the Saudi Geological Survey seismic network catalog. Black dashed lines show the plate boundaries obtained by Bird (2003). Inverted white triangles are stations used in this analysis. White square is the location of Harrat Lunayyir. Black star is the location of the 2014 Jizan earthquake (*M*4.4) with corresponding focal mechanism estimated by Abdelfattah and others (2017). *B*, Satellite image (from Esri © 2021 and its licensors) showing the epicentral distribution of events in the area of the 2009 Harrat Lunayyir seismic swarm. Red star is the mainshock and black star is the second largest event during this swarm. Both are shown with corresponding focal mechanisms (Global Centroid Moment Tensor solution).

Referenced GMPEs—BSSA14

We used the BSSA14 model (Boore and others, 2014) for active tectonic regions as the referenced GMPEs to develop the new GMPEs for western Saudi Arabia. The assumption used in this study is that Saudi Arabian GMPEs can have the same functional form as the BSSA14 model that was derived from a large dataset covering a wide range of distances and earthquake magnitudes. The GMPEs of BSSA14 are divided into the source (F_E), path (F_P), and site (F_S) effect terms:

$$\ln Y = F_E(M) + F_P(R_{JB}, M) + F_S(V_{S30}, R_{JB}, M, z_1), \tag{1}$$

where

$\ln Y$ is the natural logarithm of PGA in g (acceleration due to gravity) or PGV in centimeters per second (cm/s).

The predictor variables in this GMPE are M (magnitude), R_{JB}, V_{S30}, and z_1.

R_{JB} is the Joyner-Boore distance, which is the closest distance to the surface projection of the fault plane.

V_{S30} is the time averaged shear-wave velocity of the top 30 meters (m). V_{S30} is computed by dividing 30 m by the shear-wave travel time through the top 30 m. This parameter is widely used to evaluate the site amplification of seismic shaking and classify sites in building codes (Dobry and others, 2000; Borcherdt, 2002).

z_1 is the basin depth, which is the depth from the ground surface to $V_{S30} = 1.0$ kilometers per second (km/s).

The source term F_E in the BSSA14 model is

$$F_E(M, mech) = e_0 U + e_1 SS + e_2 NS + e_3 RS + e_4 (M - M_h) + e_5 (M - M_h)^2 \tag{2A}$$

$$(\text{if } M \leq M_h), \qquad \text{and}$$

$$F_E(M, mech) = e_0 U + e_1 SS + e_2 NS + e_3 RS + e_6 \tag{2B}$$

$$(\text{if } M > M_h),$$

where

e_0, e_1, e_2, e_3, e_4, e_5, and e_6 are source coefficients set by the user on the basis of the earthquake focal mechanism;

U (unspecified), SS (strike-slip), NS (normal-slip), and RS (reverse-slip) are the fault-type parameters, with a value of 1 or 0 if the user chooses to include each parameter or not; and

M_h is the hinge magnitude at which the equation for F_E changes from the quadratic form (eq. 2A) to the linear form (eq. 2B) with a value of $M_h = 5.5$ for PGA and 6.2 for PGV (Boore and others, 2014).

Secondly, the path effect term F_P is given by

$$F_P(R_{JB}, M) = [c_1 + c_2 (M - M_{ref})] \ln(R / R_{ref}) + c_3 (R / R_{ref}), \tag{3}$$

where

c_1 is a constant geometrical spreading coefficient,
c_2 is a magnitude-dependent geometrical spreading coefficient,
c_3 accounts for the effect of anelastic attenuation,
R_{ref} is the reference distance model coefficient, taken as 1.0 km,
M_{ref} is the reference magnitude model coefficient, taken as 4.5 (Boore and others, 2014), and

$$R = \sqrt{R_{JB}^2 + h^2}, \tag{4}$$

where

h is the finite fault effect term.

Thirdly, the site effect term F_S in the BSSA14 model uses the site amplification function of Seyhan and Stewart (2014). However, none of the stations used in this study have measured site classifications such as V_{S30} and basin depth z_1. Therefore, we assume that all the stations have a reference V_{S30} of 760 meters per second (m/s), which implies that the site effect term F_S will be ignored. Instead of the site effect term we calculate site residuals. We also estimated V_{S30} for 30 stations from the horizontal-to-vertical (H/V) response spectral ratio using the conversion equation proposed by Ghofrani and Atkinson (2014) as is discussed below.

Dataset

In recent years a dense seismic network has been deployed throughout Saudi Arabia to monitor the seismicity of the Arabia Plate. More than 180 stations of the Saudi National Seismic Network (SNSN) recorded more than 1,000 earthquakes with $M \geq 3$ between 2006 and 2016 in and around the Arabian Peninsula. Since the earthquake magnitudes are reported in local magnitude and not moment magnitude by SGS, we adopted local magnitude in this analysis. From this event catalog, we selected 217 events with good signal-to-noise ratios (SNRs) located in the Red Sea, the Gulf of Aqaba, and western Saudi Arabia, each recorded by a minimum of 5 stations (fig. 1). The 58 stations of SNSN used in this study (fig. 1) each recorded at least 5 events. These stations consist of permanent Nanometrics Trillium 120 broadband (38 stations), Trillium 40 intermediate (12 stations), and Streckeisen STS-2 broadband (8 stations) seismometers. A total of 177 events in our dataset occurred during the 2009 Harrat Lunayyir seismic swarm (Pallister and others, 2010), and the rest of the events occurred in the Red Sea, the Gulf of Aqaba, and near the border with Yemen. The 217 events we have selected vary between $M3$ and $M5.39$ including 5 events with $M > 5$. Most of the short regional distance ($R_{JB} < 50$ km) recordings from these larger earthquakes are from the $M5.18$ and $M5.39$ events, which occurred within the 2009 Harrat Lunayyir seismic swarm (shown in fig. 1B). The SGS event catalog does not include any focal mechanism information. However, more than 80 percent of the events in our dataset occurred during the 2009 Harrat Lunayyir swarm, of which several large events have normal fault mechanisms (Hansen and others, 2013); InSAR analysis and inspection of ground cracking reveal that the surface deformation during this swarm was normal faulting (Pallister and others, 2010; Jónsson, 2012). Our dataset (see "Data and Resources" section) also includes some strike-slip events along the Aqaba-Dead Sea Transform boundary, the 2014 Jizan earthquake (M_w 4.4; fig. 1A), and aftershocks that also have strike-slip fault mechanisms (Abdelfattah and others, 2017).

We selected a total of 2,770 seismograms for the final dataset after examining the SNR between the S-wave and the noise window before P-wave arrival using the method of Gupta and others (2017). The selected seismograms were bandpass filtered between 0.07 and 30 hertz (Hz) based on the instrument response and then differentiated to accelerograms.

Since some small events recorded at large distances during the 2009 Harrat Lunayyir seismic swarm are contaminated by long-period noise, we compared the high-pass filtered waveforms with two different cutoff frequencies (0.07 and 0.3 Hz) for both displacement and velocity waveforms (fig. 1.1 of appendix 1). We have determined that the long-period noise still has a somewhat higher amplitude when using the 0.07 Hz cutoff frequency but has lower amplitude when using the 0.3 Hz cutoff frequency. However, the velocity waveforms for the two different high-pass filtered cases are quite similar and such long-period noise does not affect our PGA and PGV analysis. Since the larger events have more longer period energy in their signals, we keep the bandpass filter range between 0.07 and 30 Hz.

Since a strong-motion database has not previously been available for Saudi Arabia, we created a new one to define R_{JB}, PGA, and PGV values. Our dataset has a limited magnitude range (between $M3$ and $M5.4$) and records of smaller events at long distances are contaminated by long-period noise, as described above. Therefore, we did not consider the response spectra in this study. As our dataset consists of events with $M < 5.4$, finite fault effects are ignored, and we adopted the epicentral distance as R_{JB}. Since the PSHA in Saudi Arabia is performed using area sources, not faults, the GMPEs developed with epicentral distance are easier to apply, in agreement with Bindi and others (2017). For ground-motion parameters, horizontal-component records are usually adopted to evaluate the level of building damage caused by ground shaking. However, these records are obtained from two orthogonally oriented components at a given site and depend on the orientation of the instruments. Boore (2010) solved this problem by using the two horizontal components rotated in small increments over 180 degrees (rotation-angle periodicity). We estimated PGA and PGV for all 2,770 records using RotD50 (Boore, 2010), which is the 50th-percentile (median) value of peak amplitudes obtained at all rotation angles. Figure 2 shows the data distribution of all records used in this study.

Comparison Between Observed Data and BSSA14

In this section, we quantitatively compare the observed data to the reference GMPE model (BSSA14) by evaluating the misfit between them. Since all the events in our dataset are smaller than $M5.5$, we adopted equation 2A for the source term which includes the quadratic term along with the linear term. Our dataset consists of the normal-faulting events that occurred at the extensional boundary of the Red Sea and in the volcanic lava field, Harrat Lunayyir, as well as strike-slip events that occurred along the Aqaba-Dead Sea Transform boundary and in western Saudi Arabia. Therefore, we removed the e_3 term of equation 2A to exclude reverse faulting in this analysis. In addition, since we ignore the site effect term F_S of equation 1 owing to the lack of V_{S30} values, the simplified version of the equation used in this study is as follows:
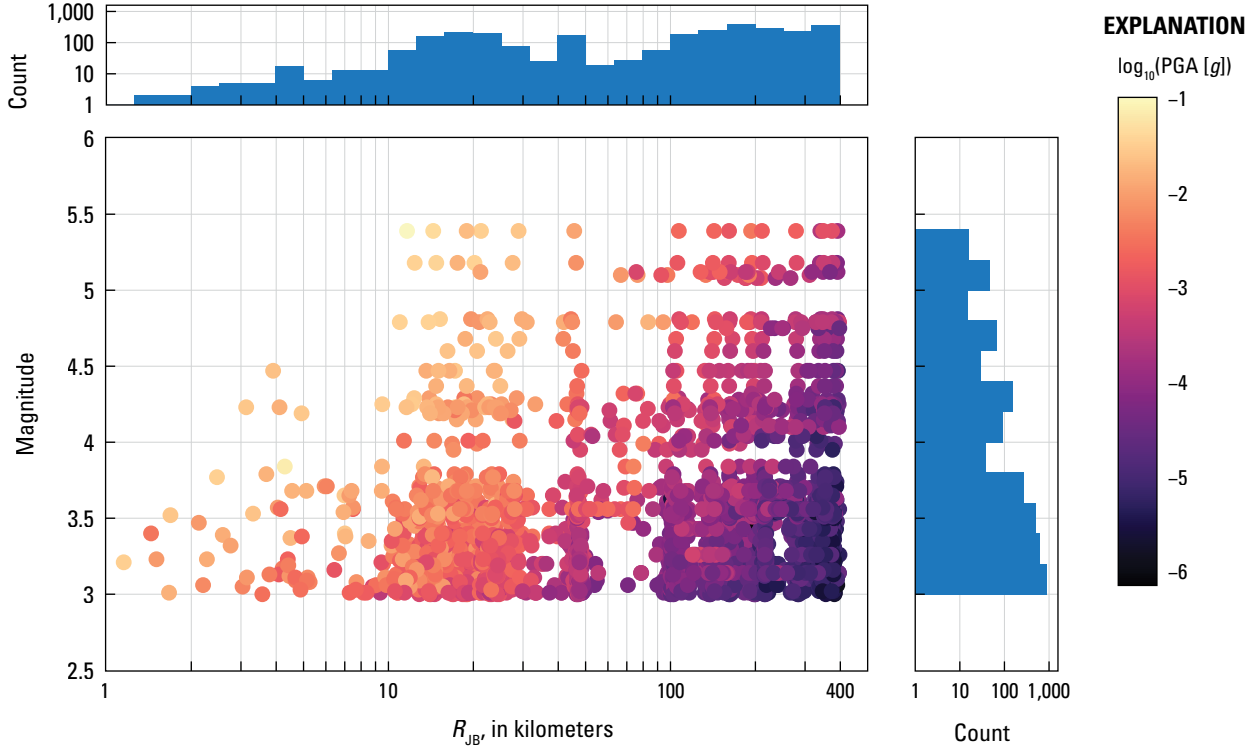
Figure 2.   Plot of magnitude versus Joyner-Boore distance (R_{JB}) showing distribution of the Saudi Arabia ground-motion dataset. Each point shows the observed record for peak ground acceleration (PGA) with colors based on the logarithm of PGA [g]. The top and right panels show the histogram of data points against distance and magnitude. g, acceleration due to gravity.

$$\ln Y(M, R_{JB}) = F_E(M) + F_P(R_{JB}, M), \text{ or} \qquad (5)$$

$$= e_0 U = e_1 SS + e_2 NS + e_4(M - M_h) + e_5(M - M_h)^2$$

$$+ [c_1 + c_2(M - M_{ref})] \ln(R/R_{ref}) + c_3(R - R_{ref}).$$

The procedure for the analysis of residuals from the observed ground-motion parameters has mostly followed the methodology of Scasserra and others (2009). To evaluate the misfit between observed ground-motion parameters and the referenced GMPE, we calculate the following residuals from the referenced GMPE:

$$(\delta_{ij})_k = \ln(Y_{ij}) - \ln(M_{ij})_k, \qquad (6)$$

where

δ_{ij} is the total observed ground-motion residual for each event i recorded at each station j,

Y_{ij} is the ground-motion parameter obtained from our dataset,

M_{ij} is the ground-motion parameter calculated from the reference GMPE, and

k is an index that refers to the different ground-motion parameters, PGA and PGV.

For the total residuals, between-event (or inter-event) variations can be separated from within-event (or intra-event) variations by performing mixed-effects regression analysis

(Abrahamson and Youngs, 1992). Total residuals can then be separated into three components:

$$(\delta_{ij})_k = c_k + (\delta E_i)_k + (\delta W_{ij})_k, \qquad (7)$$

where

c_k represents the mean offset of the data relative to the reference GMPE,

δE_i represents the event residual for event i, and

δW_{ij} represents the within-event residual for recording j of event i.

In addition, the within-event residual is the contribution of the effects of different seismic ray paths and stations (Baltay and others, 2017; Sahakian and others, 2018). Therefore, we introduced a site residual separated from the ray-path portion of the within-event residual since we do not take into account any site effects owing to the lack of V_{S30} values for all stations. Consequently, the within-event residual is separated into two components:

$$(\delta W_{ij})_k = (\delta S_j)_k + (\delta WS_{ij})_k, \qquad (8)$$

where

δS_j represents the site residual, and

δWS_{ij} represents the rest of the within-event residual, which we hereafter call the path residual following Sahakian and others (2018).

We separated these two residual components by adding the site residual as another random effect during mixed-effects regression analysis (Abrahamson and Youngs, 1992). To check for similarity of distance scaling between observed ground-motion records and the reference GMPE, we plotted the path residual δWS_{ij} with respect to R_{JB} (fig. 3). The path residuals for both PGA (fig. 3A) and PGV (fig. 3B) indicate that overall, there are no significant trends or offsets. However, path residuals of PGA and PGV for $M > 5$ events have a slight positive trend when R_{JB} is greater than 100 km (fig. 3). On the other hand, there are no such similar positive trends for

$M < 5$ events. This feature was also noticed by Gülerce and others (2016) for the within-event residuals between data from Turkey and the GMPEs of Abrahamson and Silva (2008; hereafter AS08) and Chiou and Youngs (2008; hereafter CY08). In those results, the within-event residuals at distances between 100 and 200 km show positive trend, potentially because of the ground motions recorded at distances greater than 100 km for $M4.5$–5.5 events (Gülerce and others, 2016). In general, PGA and PGV at longer distances are mainly affected by the anelastic attenuation term which corresponds to c_3 in equation 3.
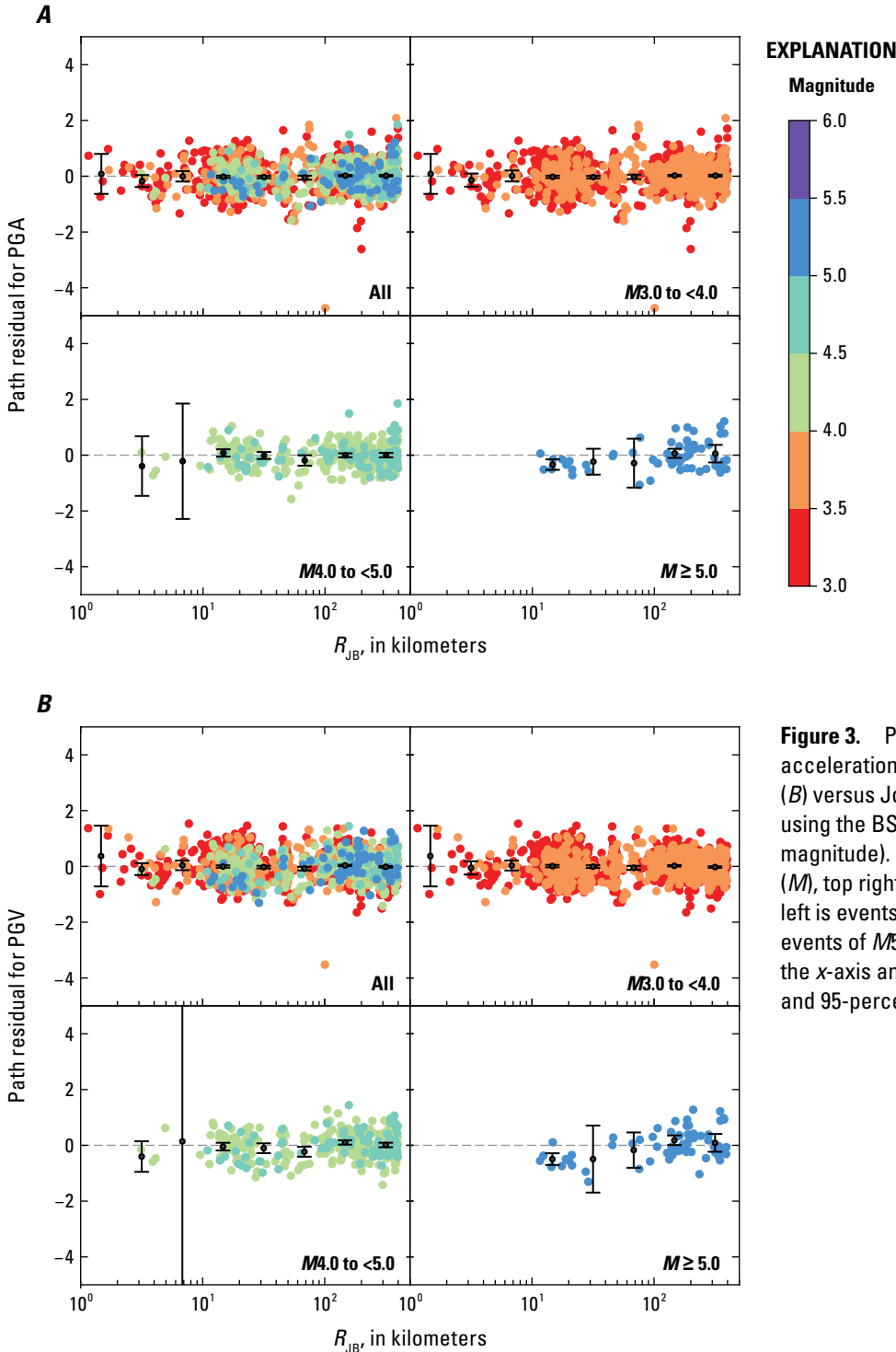
Figure 3. Plots of path residuals for peak ground acceleration (PGA) (*A*) and peak ground velocity (PGV) (*B*) versus Joyner-Boore distance (R_{JB}) calculated using the BSSA14 model (color of dots corresponds to magnitude). In parts *A* and *B*, top left is all magnitudes (*M*), top right is events between *M*3 and *M*4, bottom left is events between *M*4 and *M*5, and bottom right is events of *M*5 and larger. Residuals are binned along the *x*-axis and bin medians are shown by their mean and 95-percent confidence intervals.

To compare the magnitude scaling between the observed data and the reference GMPE, we plotted the event residuals δE_i with respect to the magnitude of each event (fig. 4). For PGA records, the event residuals for M4–5.5 events show negative values as well as a negative trend, whereas M3–4 events have smaller event residuals with perhaps a small positive trend. These features imply that the actual magnitude scaling for larger observed events is significantly less than the scaling employed by the BSSA14 model. In contrast, the event residuals for PGV data are close to zero for $M < 4.5$ events. However, they are widely scattered for larger events. Therefore, it is important to modify the reference GMPE, especially for an event with $M > 5$. Such an event, which could cause significant damage to infrastructure, may be considered as a possibility in western Saudi Arabia based on the instrumental and historical records (Ambraseys and others, 2005). Since R_{JB} is measured from the surface projection of the fault to the station, source depth is not considered. Therefore, we also plotted the event residuals δE_i with respect to the focal depth of each event (fig. 1.2 of appendix 1). However, a trend or offset of event residuals with depths shallower than 20 km is absent for PGA and PGV, as indicated by Boore and others (2014).

Regression Analysis

The trial-and-error regression analysis (Baker and others, 2021) applied to our dataset revealed that the magnitude-dependent geometrical spreading term c_2 was poorly constrained, possibly because of the lack of records at shorter distances for large events. The geometrical spreading term of GMPEs dominates at shorter distances, and a sufficient number of regional records with a wide range of magnitude events are necessary to constrain c_2. Therefore, we adopted the value of c_2 from the original BSSA14 model for use in our modified GMPE. In addition, owing to the tradeoff between c_1 and c_3, we divided multiple steps for regressively fitting the data in a similar way as BSSA14. As a first step, we evaluated the anelastic attenuation term c_3, which is relatively independent of magnitude (Boore and others, 2014) and better resolved than c_1 owing to a larger amount of data recorded at longer distances. The rest of the coefficients (c_1, e_0, e_1, e_2, e_4, and e_5) were then adjusted by a regressive fit to the seismic recordings in Saudi Arabia.

The anelastic attenuation term primarily affects longer distance records, whereas the geometrical spreading term affects the shorter distance records. In the first step of our
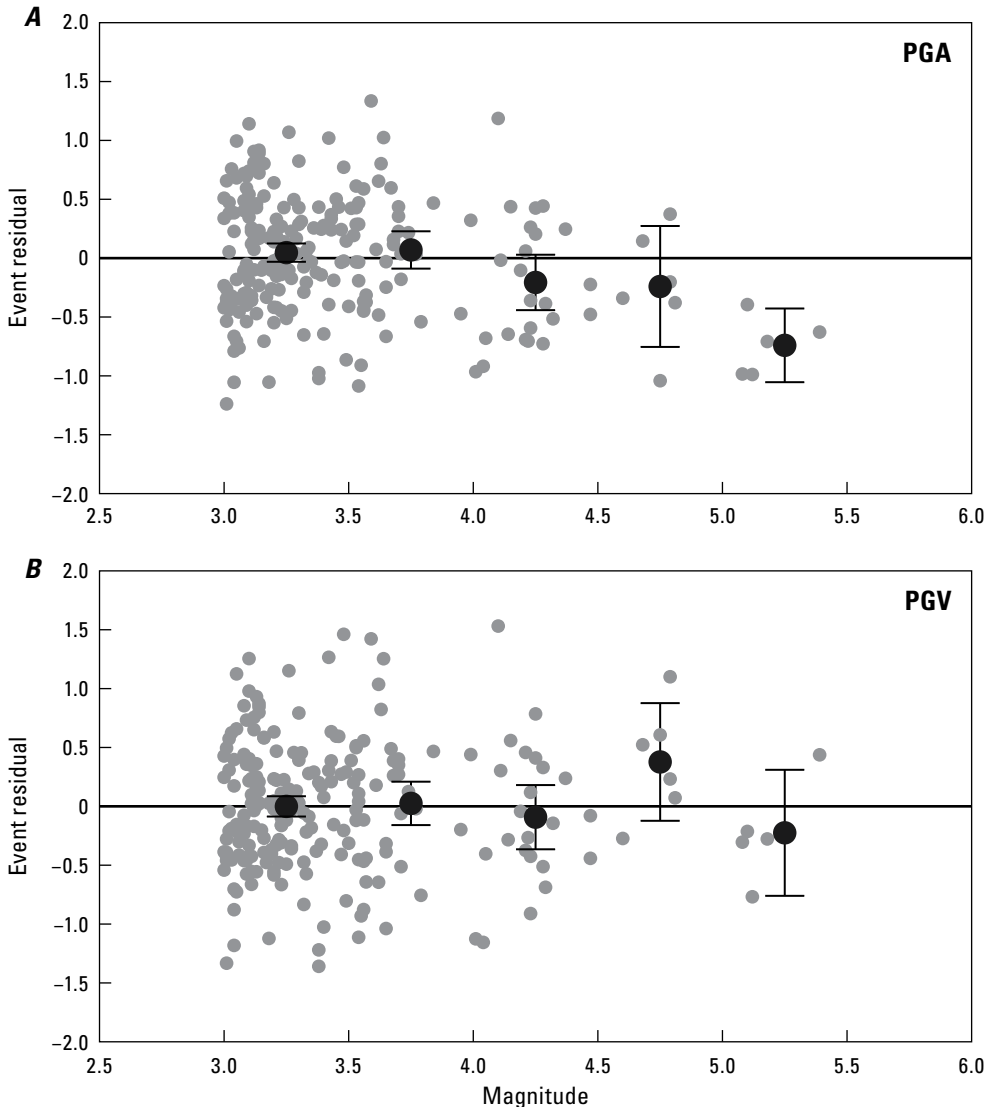
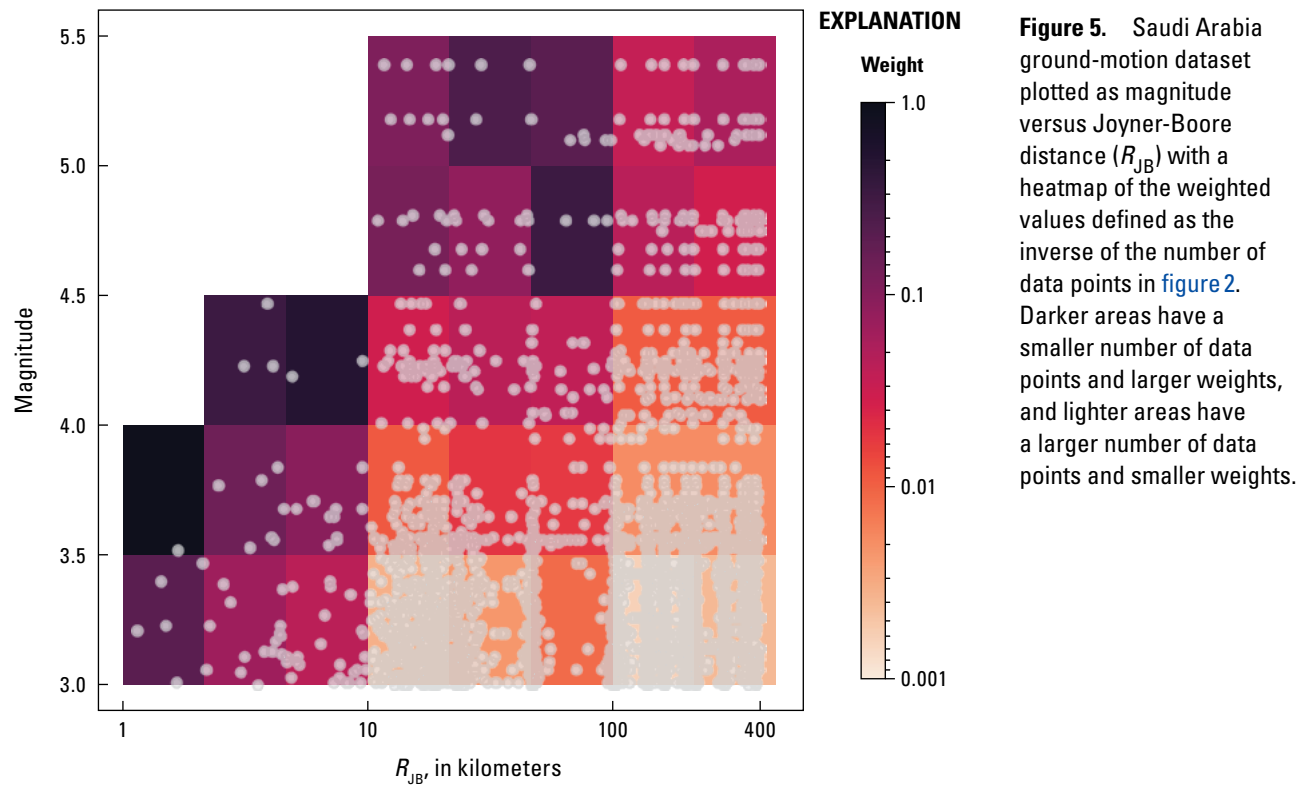**Figure 4.** Plots of event residuals for peak ground acceleration (PGA) (*A*) and peak ground velocity (PGV) (*B*) versus magnitude from the BSSA14 model. Residuals are binned along the *x*-axis and bin medians are shown by their mean and 95-percent confidence intervals.

regressive fit, we limited the records of events to those that have at least two records each for closer ($R_{JB} \leq 50$ km) and farther ($R_{JB} \geq 100$ km) distances to obtain a better estimate of c_3. Using this limited dataset, we performed a mixed-effects regression analysis using equation 5. Unlike the situation for the NGA-West2 project that had abundant available data, the difficulty in developing GMPEs in other areas arises from the limited number of ground-motion recordings. Although the recently expanded seismic network in Saudi Arabia has greatly improved coverage of the Arabian Peninsula, the ground-motion database is not yet as complete as other active tectonic regions such as California, Japan, and Italy. In particular, there is a lack of recordings of large events at short distances.

The weighted regression values presented here are estimated based on the density of the measurements in the data distribution (fig. 2). We divided the data into bins of R_{JB} and magnitude that appear as blocks in the data distribution and calculated the weighted values using the reciprocal of the

number of data points in each block as the weighting factors (fig. 5). Using equation 5, we then evaluated the source term coefficients e_2, e_4, and e_5, and the geometrical spreading term c_1 using these weighted values and the fixed value of c_3 obtained in the first step. Since we have a limited amount of data, especially for large events recorded at short distances, this weighting scheme is helpful for more robust constraints in both magnitude and distance scaling.

In order to develop regional GMPEs in western Saudi Arabia, we performed a mixed-effects regression analysis on the entire dataset. Table 1 compares the coefficients for BSSA14 and Saudi Arabian GMPEs presented here for PGA and PGV. The path residuals (fig. 6) and event residuals (fig. 7) between the data and the modified Saudi Arabian GMPEs were also obtained from the mixed-effects regression results. The mean event residuals for PGA generally became somewhat smaller and do not appear to have a magnitude scaling trend (fig. 7A). This situation is

Figure 5. Saudi Arabia ground-motion dataset plotted as magnitude versus Joyner-Boore distance (R_{JB}) with a heatmap of the weighted values defined as the inverse of the number of data points in figure 2. Darker areas have a smaller number of data points and larger weights, and lighter areas have a larger number of data points and smaller weights.

Table 1. The equation coefficients of BSSA14 and the best model of Saudi Arabian ground-motion prediction equations for both peak ground acceleration (PGA) and peak ground velocity (PGV).

Model	Coefficient							
	e_0	e_1	e_2	e_4	e_5	c_1	c_2	c_3
PGA (BSSA14)	0.447	0.486	0.246	1.43	0.0505	−1.13	0.192	−0.0081
PGA (best model)	−1.24	−0.897	−0.920	0.26	−0.222	−0.96	0.192	−0.0073
PGV (BSSA14)	5.04	5.08	4.85	1.07	−0.154	−1.24	0.149	−0.0034
PGV (best model)	4.09	4.38	4.23	0.75	−0.198	−1.28	0.149	−0.0016
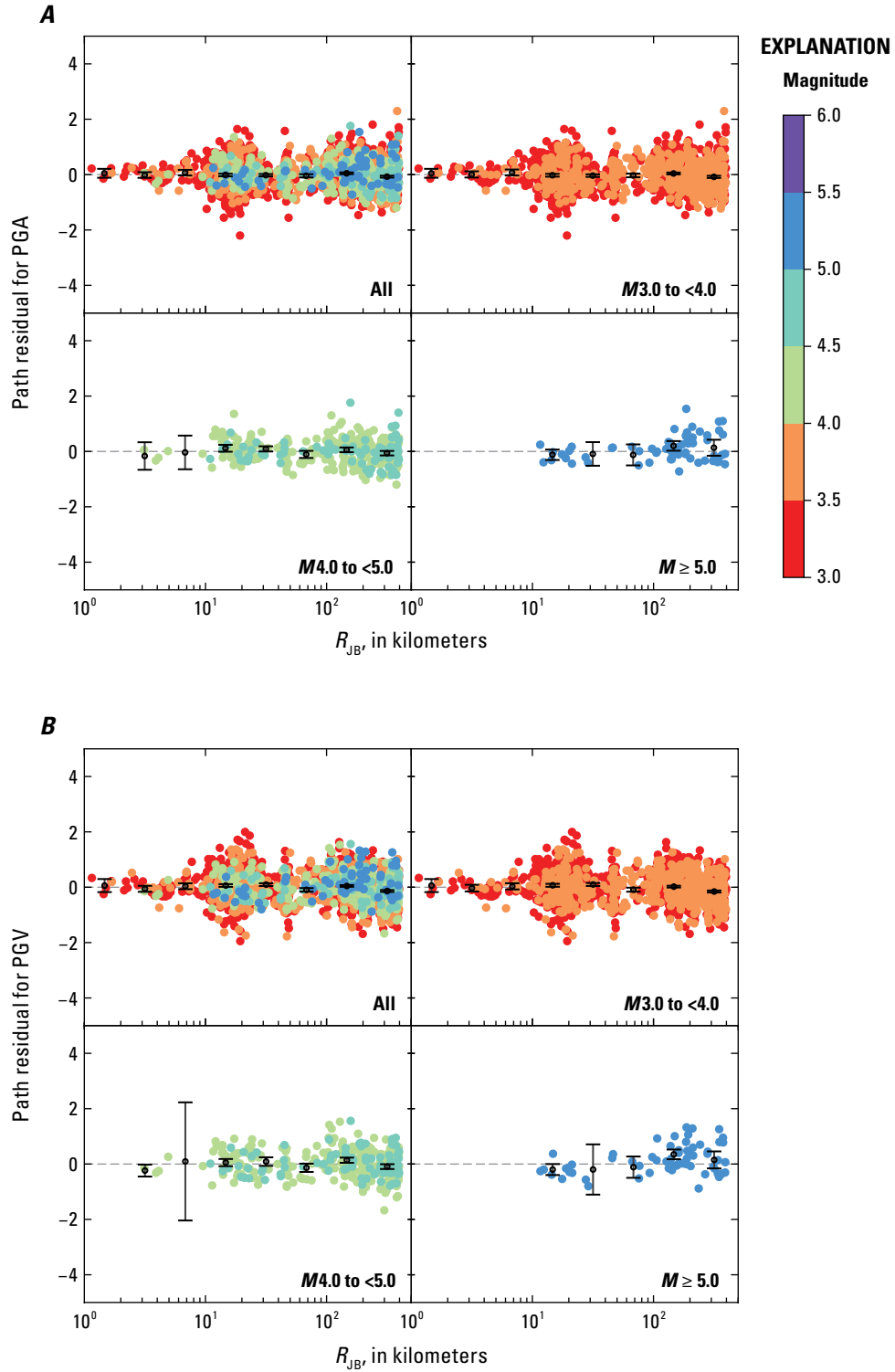
Figure 6. Plots of path residuals for peak ground acceleration (PGA) (*A*) and peak ground velocity (PGV) (*B*) versus Joyner-Boore distance (R_{JB}) from the Saudi Arabian ground-motion prediction equations (GMPEs) (color of dots corresponds to magnitude). In parts *A* and *B*, top left is all magnitudes (*M*), top right is events between *M*3 and *M*4, bottom left is events between *M*4 and *M*5, and bottom right is events of *M*5 and larger. Residuals are binned along the *x*-axis and bin medians are shown by their mean and 5-percent confidence intervals.
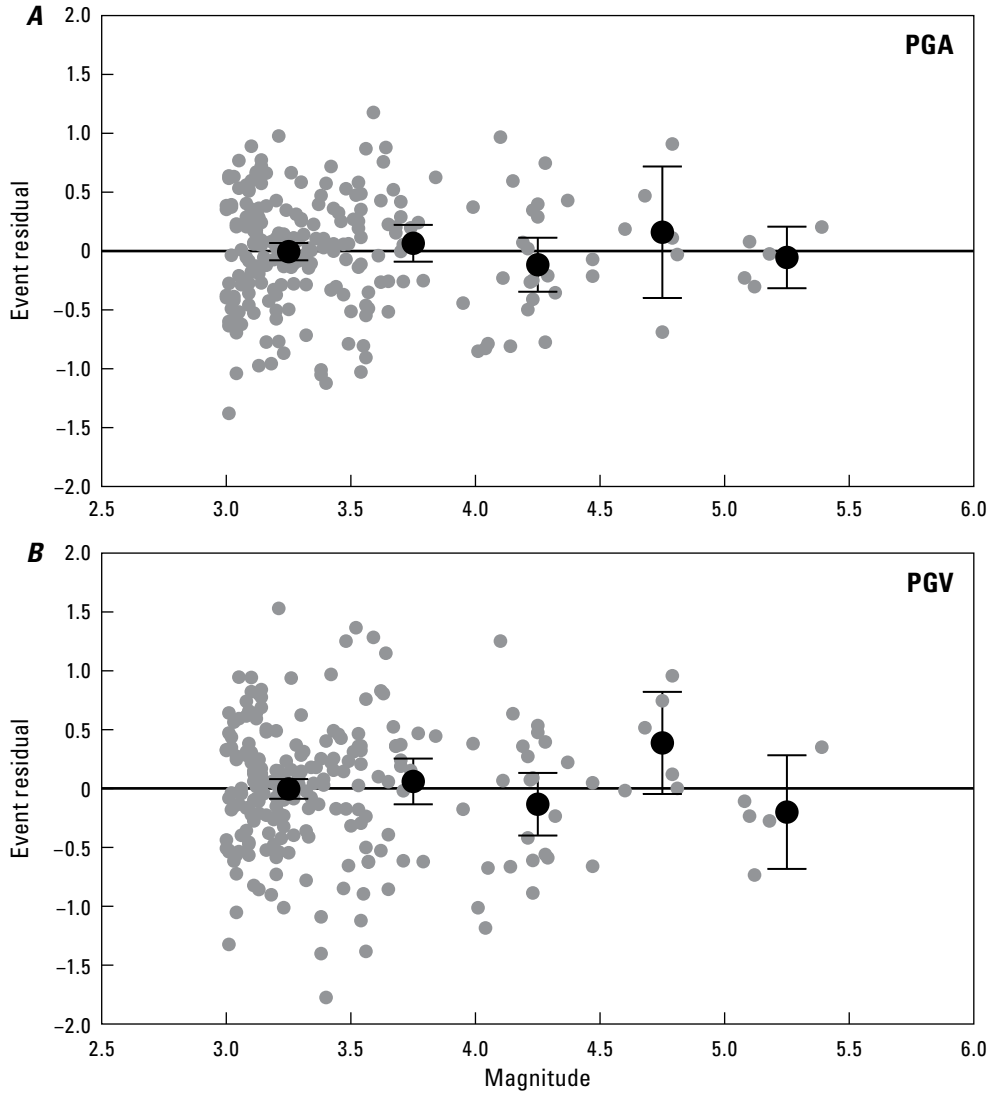
Figure 7. Plots of event residuals versus magnitude for peak ground acceleration (PGA) (*A*) and peak ground velocity (PGV) (*B*) from the Saudi Arabian ground-motion prediction equations (GMPEs). Residuals are binned along the *x*-axis and bin medians are shown by their mean and 95-percent confidence intervals.

controlled by decreasing the values of e_4 and e_5 as shown in table 1. Note that the e_5 coefficient for the quadratic term in magnitude scaling for PGA changed from positive in BSSA14 to negative in the Saudi Arabian GMPEs. This negative quadratic feature is consistent with the magnitude scaling obtained by Baltay and Hanks (2014) using an earthquake source model in the range $3.3 < M < 4.5$ (Brune, 1970) and $4.5 < M < {\sim}6.5$ (Hanks and McGuire, 1981; Boore, 1983). Therefore, the magnitude scaling of our modified GMPE appears to be more appropriate for Saudi Arabia. We also find no trends or offsets of the event residuals from the Saudi Arabian GMPEs with source depth (fig. 1.2 of appendix 1). Although there are only minor differences for the path residuals for both PGA and PGV between BSSA14 and the Saudi Arabian GMPEs, they are improved for $M > 5$ events (fig. 6). The path residuals from the Saudi Arabian GMPEs at shorter distance ranges are also improved compared to the residuals from BSSA14 (fig. 6) and have an improved magnitude scaling trend for PGA (fig. 7). These refinements in the Saudi Arabian GMPEs will improve the accuracy of seismic hazard assessments for western Saudi Arabia.

Extrapolation on Magnitude Scaling and Model Smoothing

Since the magnitudes of the events used in this study range from $M3$ to 5.5, we need to extrapolate to account for larger magnitude events. This is especially important in order to apply our new GMPEs to the PSHA for Saudi Arabia. The maximum magnitude of events in the volcanic fields and offshore in the Red Sea are assumed to be 6.0 and 7.3, respectively (Zahran and others, 2016). In addition, volcanic earthquakes have a potential to be as large as $M7$ like the Hawaiian earthquakes in 1975 (surface-wave magnitude [M_s] 7.1; Eissler and Kanamori, 1987) and 2018 (M_w 6.9; Kehoe and others, 2019). It is difficult to constrain the magnitude scaling for the GMPEs owing to the lack of recorded larger events, so we assume that the trends of the magnitude scaling in large magnitude range are the same as for the BSSA14 model. In the BSSA14 model, the source term for a magnitude larger than the hinge magnitude is defined as a linear function so we also change the functional form of our GMPEs:

$$\ln Y(M, R_{JB}) = F_E(M) + F_P(R_{JB}, M) \tag{9}$$

$$= e_0 U = e_1 NS = e_6 (M - M_h)$$

$$+ [c_1 + c_2 (M - M_{ref})] \ln\left(\frac{R}{R_{ref}}\right) c_3 (R - R_{ref})$$

$$(\text{if } M > M_h),$$

where

e_6 is the coefficient of the linear magnitude scaling term, which is the same value as for the BSSA14 model.

The other coefficients are the same values estimated previously in this study. Many different GMPEs, including BSSA14, have adopted a hinge magnitude to constrain the magnitude scaling into two or more regression segments. This means that the trend of magnitude scaling is modeled as changing abruptly at $M_h = 5.5$ for PGA and 6.2 for PGV. However, the hazard analysis for a region of low to moderate seismicity would be affected by magnitude scaling around $M5.5$ to 6 as mentioned by Bindi and others (2017). Therefore, we estimate the interpolation function needed to make a smooth transition at the hinge magnitude, as suggested by Baltay and Hanks (2014). Since we need four boundary conditions that have the same values and trends as the two regression segments at both ends of the interpolation function, the interpolation function is defined as a cubic equation. The interpolation function of magnitude scaling is therefore given by

$$F_E^{\text{interp}}(M) = p_0 + p_1 (M - M_h) + p_2 (M - M_h)^2 + p_3 (M - M_h)^3, \tag{10}$$

where

$p_0, p_1, p_2,$ and p_3 are model coefficients estimated through the four boundary conditions and defined using e_4, e_5, e_6, and M_h.

In this study, we apply the interpolation function from $M = M_h - 0.5$ to $M_h + 0.5$, and the model coefficients of the interpolation function for the functional form of the BSSA14 model are as follows:

$$p_0 = \frac{-e_4 + e_6}{8}, \tag{11A}$$

$$p_1 = \frac{4e_5 + e_5 + e_6}{8}, \tag{11B}$$

$$p_2 = \frac{-e_4 + e_5 + e_6}{2}, \text{ and} \tag{11C}$$

$$p_3 = \frac{e_5}{2} \tag{11D}$$

Therefore, we redefine the source term:

$$F_E(M) = e_0 U + e_1 SS + e_2 NS + p_0 = p_1 (M - M_h) + e_5 (M - M_h)^2 \tag{12A}$$

$$(\text{if } M \leq M_h - 0.5),$$

$$F_E(M) = e_0 U + e_1 SS + e_2 NS + p_0 = p_1 (M - M_h) + p_2 (M - M_h)^2 + p_3 (M - M_h)^3 \tag{12B}$$

$$(\text{if } M_h - 0.5 < M \leq M_h + 0.5), \text{ and}$$

$$F_E(M) = e_0 U + e_1 SS + e_2 NS + e_6 (M - M_h) \tag{12C}$$

$$(\text{if } M > M_h + 0.5).$$

The smoothed magnitude scaling GMPE for PGA and PGV is similar to the unsmoothed magnitude scaling of the GMPE. However, the predicted values of PGA and PGV for the smoothed model are smaller at larger magnitudes than they would be if the GMPEs determined by our dataset were extrapolated to $M7$ (fig. 8).

A

B
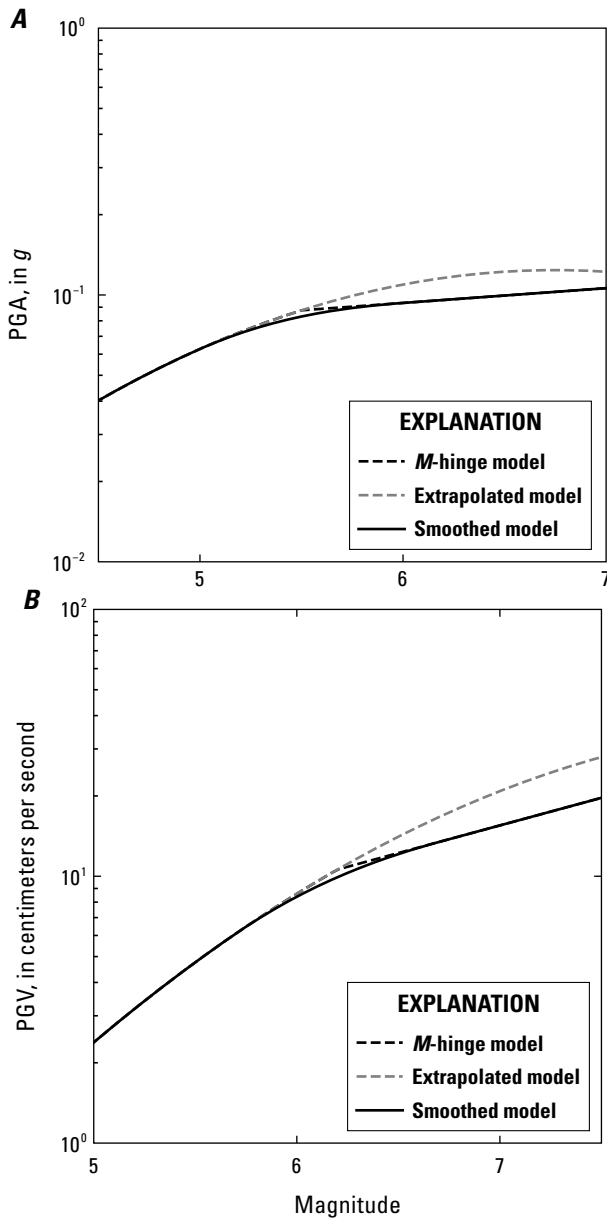
Figure 8.   Plots of peak ground acceleration (PGA) (*A*) and peak ground velocity (PGV) (*B*) versus magnitude (*M*), comparing the smoothed model with the magnitude-hinge (*M*-hinge) and extrapolated model. M_h is the hinge magnitude at which the equation for F_E changes from the quadratic form (eq. 2*A*) to the linear form (eq. 2*B*) with a value of M_h = 5.5 for PGA and 6.2 for PGV (Boore and others, 2014). PGA is about 18–24 percent smaller and PGV is about 4–16 percent smaller in the smoothed model than in the extrapolated model in the range of *M*6–6.5. *g*, acceleration due to gravity.

Comparison of Saudi Arabian GMPEs with BSSA14 and Other GMPEs

Figure 9 shows the Saudi Arabian GMPEs with the observed data and the BSSA14 model for four different magnitude events (*M*3.25, *M*4.25, *M*5.25, and *M*6.5; see also figs. 1.3 and 1.4 of appendix 1). The Saudi Arabian GMPEs are in good agreement with the observed ground motions for PGA and PGV particularly with respect to distance decay. In comparison with BSSA14, the Saudi Arabian GMPEs have a lower rate of distance decay at distances between 10 and 400 km for PGA and between 100 and 400 km for PGV. This is due to the lower geometrical spreading for PGA and the lower anelastic attenuation for PGA and PGV, as compared with BSSA14. However, the main differences between the Saudi Arabian GMPEs and BSSA14 are identified in the PGA case. Note that PGAs at local distances (0 to 10 km) predicted by the Saudi Arabian GMPEs are larger for *M*3.25 and *M*4.25 but are smaller for *M*5.25 than those of BSSA14. This is due to the smaller magnitude scaling of the Saudi Arabian GMPEs. In figure 10, we compare the Saudi Arabian GMPEs with the observed data and the BSSA14 model at four different distances (10, 30, 100, and 300 km). As is evident in figure 9, the main differences between the Saudi Arabian GMPEs and BSSA14 are in the PGA values. As mentioned above, the magnitude scaling of the Saudi Arabian GMPEs is also smaller than that of BSSA14, especially for PGA. Furthermore, the PGA curves of Saudi Arabian GMPEs have larger curvature than those of BSSA14. These features correspond to the smaller magnitude-scaling coefficients e_4 and e_5 for the Saudi Arabian GMPEs than for the BSSA14 model. This causes PGAs predicted by the Saudi Arabian GMPE to be larger for *M* < 5 and smaller for *M* > 5 than those of BSSA14. These differences of magnitude scaling may arise from the different geologic setting of the BSSA14 model (appropriate for an active tectonic region) compared to our Saudi Arabian GMPEs (a volcanic region with shield-type crystalline crust). Another possible cause of the discrepancy in magnitude scaling is the difference in magnitude scales of the available datasets for each study: BSSA14 uses moment magnitude whereas our Saudi Arabian GMPEs use local magnitude. The difference between local magnitude and moment magnitude is relatively greater for the smaller (*M* < 4) events that make up most of our dataset (Munafò and others, 2016).

The modified Saudi Arabian GMPEs are also compared with other GMPEs developed for volcanic or extensional regimes in figure 11. The ground motions compared are the PGA and PGV predicted from Atkinson (2010; A10 for Hawai'i) for shallow events (depth <20 km) and from
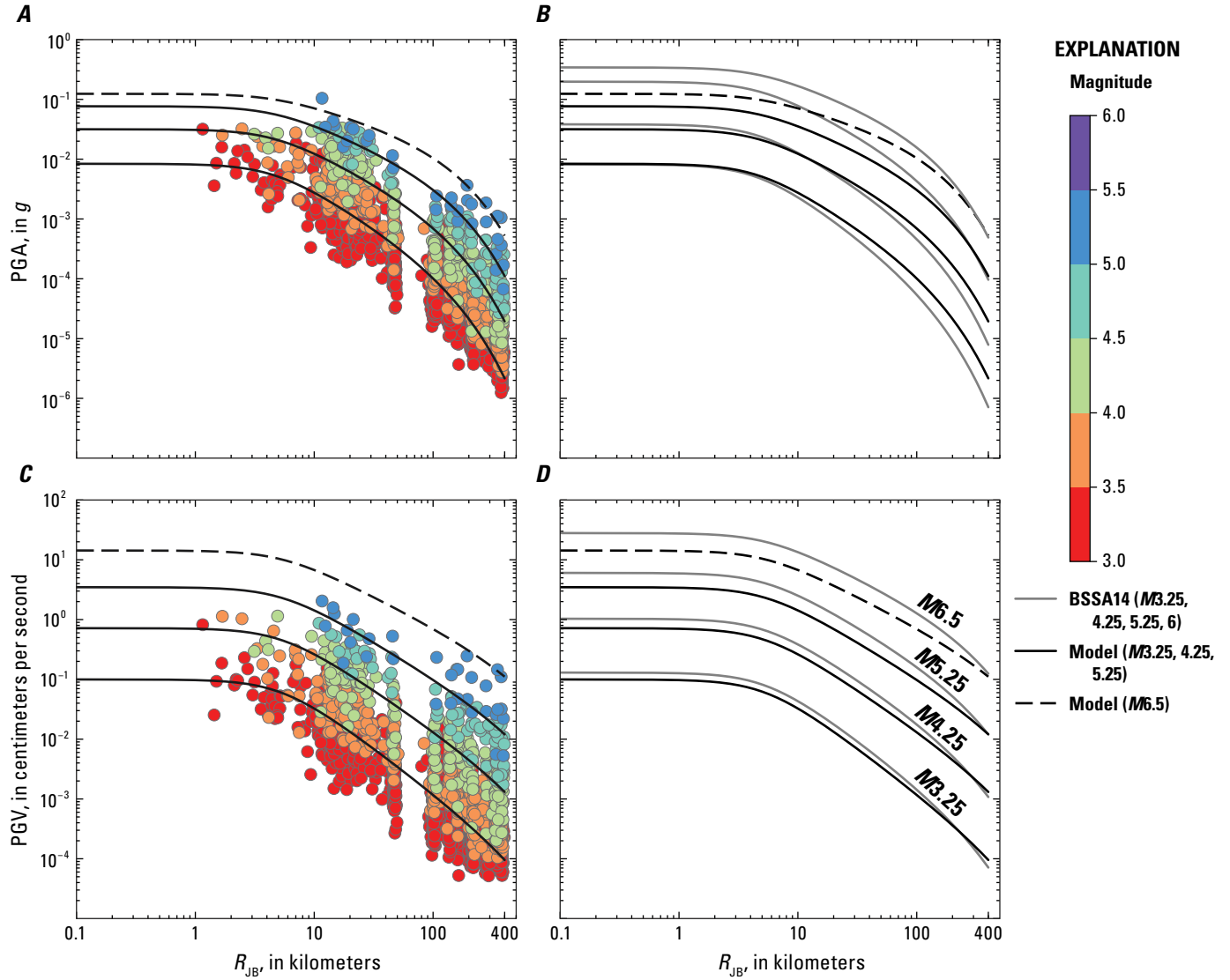
Figure 9.   Plots of peak ground acceleration (PGA) (*A, B*) and peak ground velocity (PGV) (*C, D*) versus Joyner-Boore distance (R_{JB}) comparing events with normal fault mechanisms from the Saudi Arabian ground-motion prediction equations (GMPEs) (black lines) with observed data (left, color of dots corresponds to magnitude) and the BSSA14 model (right, gray lines). Curves for Saudi Arabian GMPEs and the BSSA14 model show *M*3.25, *M*4.25, and *M*5.25 (solid) and *M*6.5 (dashed) earthquakes. *g*, acceleration due to gravity.
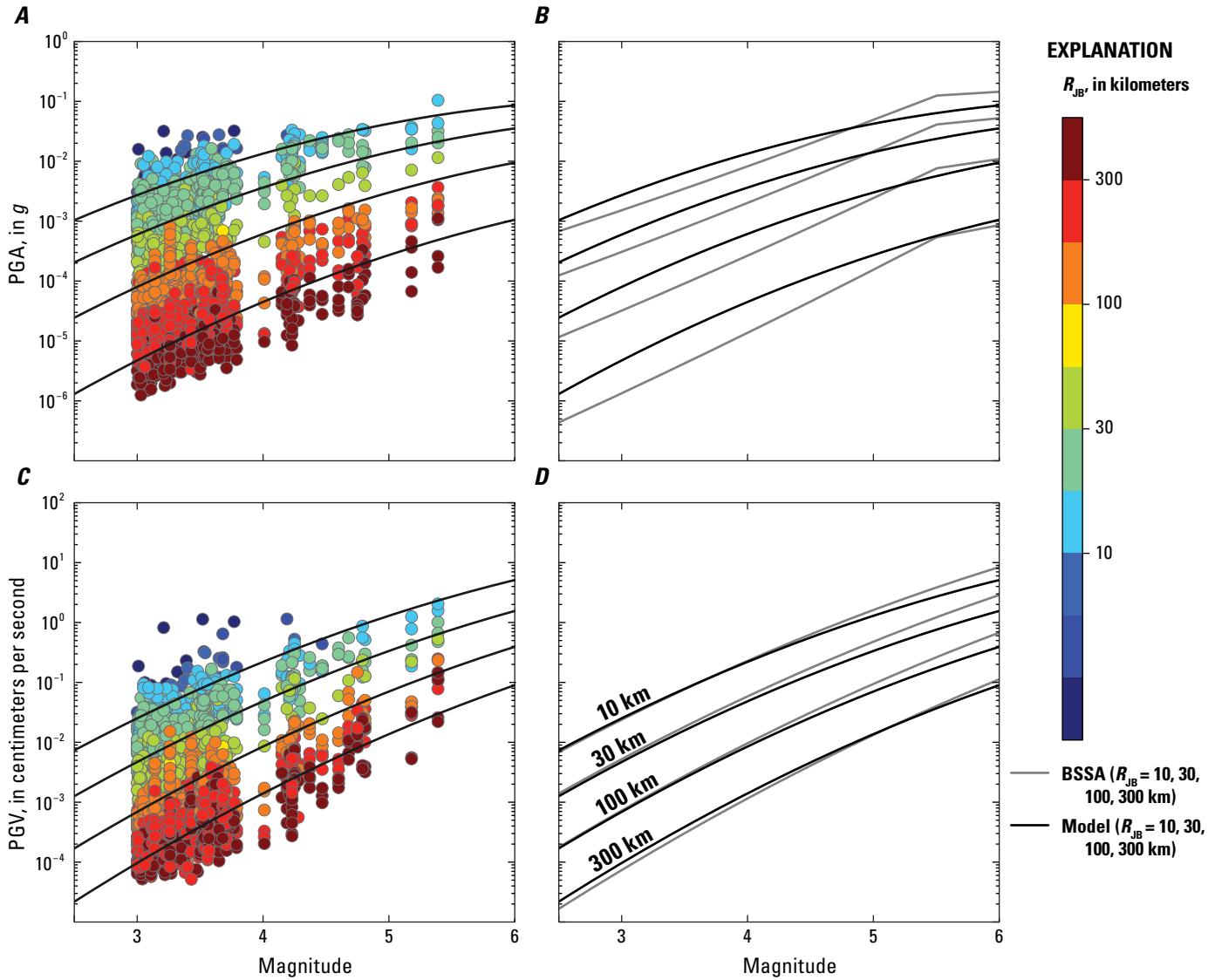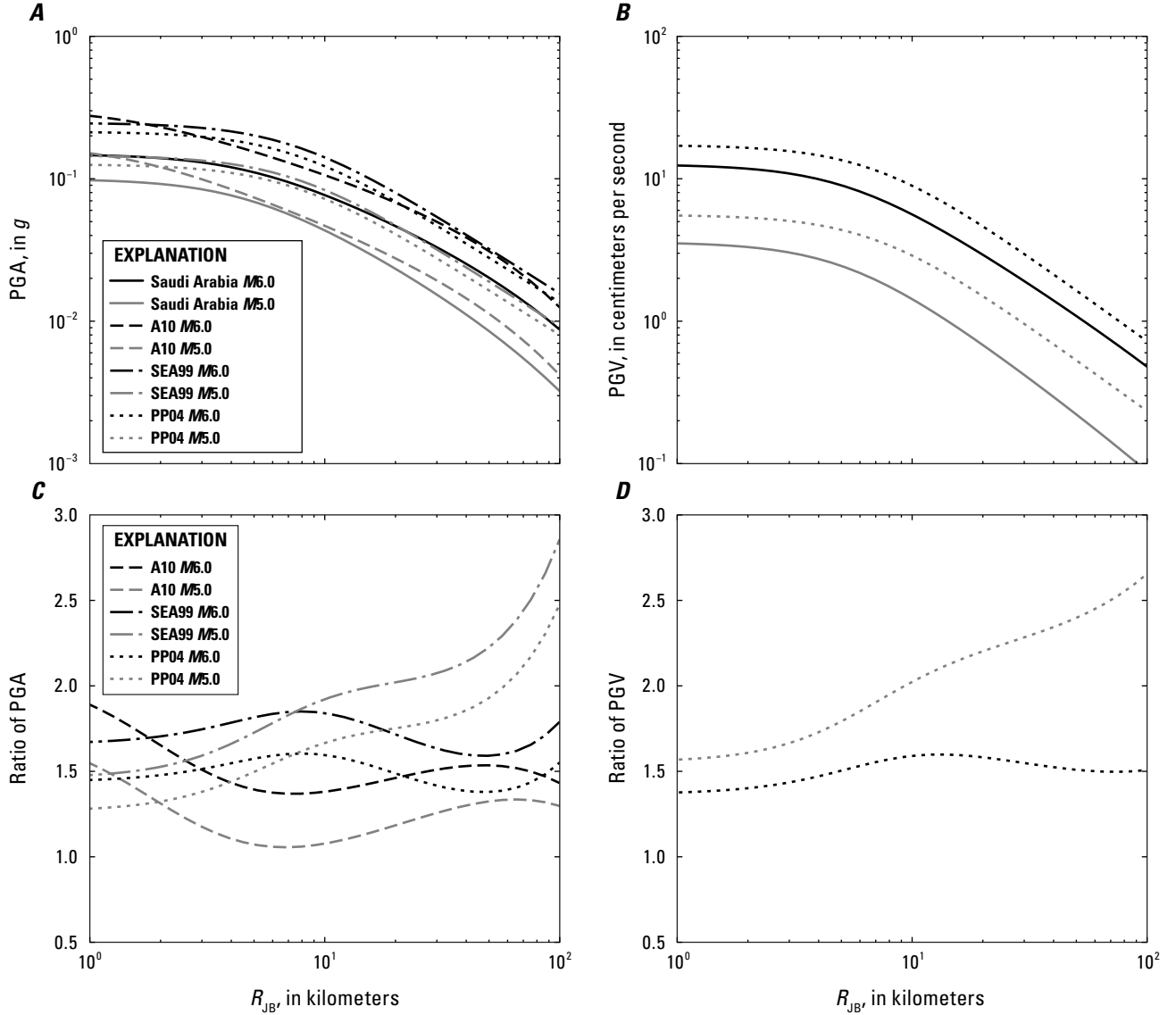
Figure 10.   Plots of peak ground acceleration (PGA) (*A, B*) and peak ground velocity (PGV) (*C, D*) versus magnitude (*M*) comparing events with normal fault mechanisms from the Saudi Arabian ground-motion prediction equations (GMPEs) (black lines) with observed data (left, color of dots corresponds to distance) and the BSSA14 model (right, gray lines). Curves for Saudi Arabian GMPEs and the BSSA14 model show Joyner-Boore distances (R_{JB}) of 10, 30, 100, and 300 kilometers (km). *g*, acceleration due to gravity.

Pankow and Pechmann (2004; PP04) and Spudich and others (1999; SEA99) for extensional regimes. The predicted PGAs of the Saudi Arabian GMPEs for both *M*5 and *M*6 events are smaller than those of the other three GMPEs. However, the A10 GMPE predicts similar PGAs for *M*5 events for distances greater than 5 km. The Saudi Arabian GMPEs have a higher rate of distance scaling than the PP04 and SEA99 GMPEs for *M*5 events but not for *M*6 events. This is due to the higher anelastic attenuation rate and the incorporation of a magnitude-dependent geometrical spreading term compared to the PP04 and SEA99 GMPEs. The difference between PGAs predicted by the Saudi Arabian GMPEs and the PP04 and SEA99 GMPEs is a factor of 1.4–1.9 except for *M*5 events at

longer distances. The predicted PGVs of the Saudi Arabian GMPEs also show a lower level and a higher rate of distance scaling for *M*5 events than those of the PP04 GMPE. We note that in comparison with the Saudi Arabian GMPEs, the PP04 estimates are (1) from 1.6 (R_{JB} = 0 km) to 2.6 (R_{JB} = 100 km) times larger for *M*5 events and (2) about 1.5 times larger for *M*6 events than the Saudi Arabian GMPEs.

In terms of seismic hazard analysis, such as PSHA, smaller magnitude events have a greater contribution to the probabilities (for example, 2 percent probabilities in 50 years) for lower seismic intensity ground shaking. Likewise, larger magnitude events have a greater contribution to the probabilities for higher seismic intensity ground shaking (Baker and
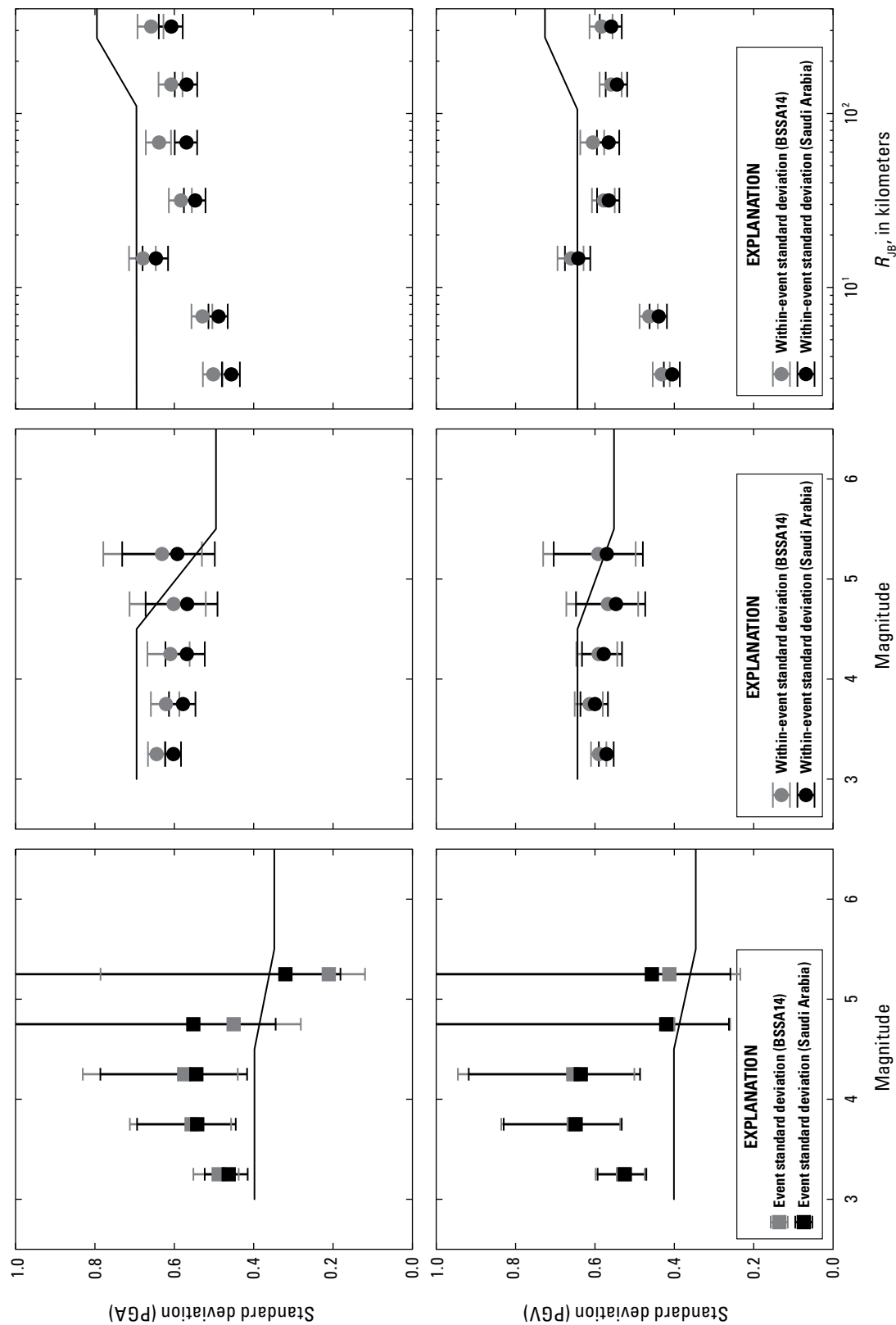
Figure 11. Top, Plots of peak ground acceleration (PGA) (*A*) and peak ground velocity (PGV) (*B*) versus Joyner-Boore distance (R_{JB}) comparing magnitude (*M*) 5.0 and 6.0 events with normal fault mechanisms from the Saudi Arabian ground-motion prediction equations (GMPEs) with Atkinson (2010; A10) for cohesive soil site conditions, and with Pankow and Pechmann (2004; PP04) and Spudich and others (1999; SEA99) for hard rock sites. Bottom, Plots of the ratio of PGA (*C*) and PGV (*D*) of each of the three other GMPEs to the Saudi Arabian GMPEs versus Joyner-Boore distance. *g*, acceleration due to gravity.

others, 2021). Therefore, the probabilities of lower to moderate seismic intensities would be higher for all distances from 10 to 300 km, whereas the probability of higher seismic intensities would be lower at shorter distances ($R_{JB} < 30$ km).

Although we previously discussed the mean of the event and path residuals, their standard deviations are important factors in understanding the quality of seismic hazard calculations such as PSHA. In Saudi Arabia, Zahran and others (2015, 2016) performed PSHA calculations using alternative GMPEs developed for regions outside of Saudi Arabia. We calculated the standard deviations of both event (inter-event) and within-event (intra-event) residuals for the Saudi Arabian GMPEs in comparison with BSSA14 (fig. 12).

For PGA and PGV, the event standard deviations obtained from the Saudi Arabian GMPEs are somewhat larger than the standard deviations of the BSSA14 model. This feature of event residuals agrees with previous studies in which the standard deviations of modified GMPEs are larger than those of their reference GMPEs (for example, Gülerce and others, 2016). This may be due to the lower number of observations used in this study compared to NGA-West2, or the difference of inherent variability in event residuals between Saudi Arabian earthquakes and the earthquakes from other regions that appear in the NGA-West2 dataset. However, it is difficult to assess which factor contributes more to the larger event standard deviations found for the Saudi Arabian GMPEs.

Figure 12.   Plots of standard deviation for peak ground acceleration (PGA) (top) and peak ground velocity (PGV) (bottom) versus magnitude (left, center) and Joyner-Boore distance (R_{JB}) (right) showing magnitude-dependent event standard deviation (left), magnitude-dependent within-event standard deviation (center), and distance-dependent within-event standard deviation (right). Grey and black symbols represent the standard deviations of each residual for the observed ground motions obtained from the BSSA14 model and from the Saudi Arabian ground-motion prediction equations, respectively. Their error bars show the 95-percent confidence intervals of the standard deviations in each magnitude and distance bin. Black lines represent the original standard deviations of the BSSA14 model.

Therefore, as with previous studies, we recommend adopting the original event standard deviations obtained by BSSA14 rather than those of the modified model for use in seismic hazard analysis. In contrast, the within-event standard deviations obtained from the Saudi Arabian GMPEs are smaller than the original within-event standard deviations of BSSA14 with respect to both magnitude and R_{JB} (fig. 12). No correction was made in this study for local site effects. Such corrections are commonly based on V_{S30} values, and these values have not been measured in the region. Hence, the original site standard deviations of BSSA14 might be smaller than those of the Saudi Arabian GMPEs, if the within-event standard deviations are divided into site and path standard deviations in the original BSSA14 model. Therefore, path standard deviations of the Saudi Arabian GMPEs should be smaller than those of BSSA14. This is possibly because the NGA-West2 database consists of a global dataset and many different regional path residuals are included in the whole path standard deviations. In contrast, the within-event standard deviations of the Saudi Arabian GMPEs are also slightly smaller than those obtained from BSSA14. Additionally, the within-event standard deviations for short distances (fig. 12) are smaller than those from the BSSA14 model, possibly owing to the heavily weighted values for these data. Since the within-event standard deviations of the Saudi Arabian GMPEs are similar to the original values of BSSA14, we also recommend using the original within-event standard deviations obtained by BSSA14 rather than those of the modified model.

Relation of GMPEs to Tectonic Setting

In the development of our modified GMPEs for Saudi Arabia, we estimated c_3, which is related to anelastic attenuation. Compared to the value of c_3 of the BSSA14 GMPEs, the estimated c_3 in this study is larger for both PGA and PGV. Therefore, the anelastic attenuation in western Saudi Arabia would be lower than in the regions where BSSA14 was originally developed, such as California. The formulation of amplitude decay with distance owing to anelastic attenuation is described as $\exp\left(-\dfrac{\pi f R}{\beta Q}\right)$ with frequency f, shear wave velocity β, and seismic quality factor Q (see, for example, Aki and Richards, 1980). When we consider a simple functional form for a GMPE (such as Baltay and Beroza, 2013), the coefficient c_3 is

$$c_3 = -\frac{\pi f}{\beta Q}. \tag{13}$$

Therefore, Q is described as

$$Q = -\frac{\pi f}{\beta c_3}. \tag{14}$$

In order to search for the dominant frequencies of the waveforms used in developing the Saudi Arabian GMPEs, we estimated the Fourier spectrum for all long-distance ($R_{JB} \geq 200$ km) waveforms from acceleration records (Baker and others, 2021). We adopt this approach because the anelastic attenuation term in the GMPEs is mainly constrained by long-distance records. As is evident from the Fourier spectra, the dominant frequency from the acceleration records is around 8–10 Hz (fig. 1.5 of appendix 1). Since the coefficient c_3 of our modified model is −0.0073, the term Q is equal to 368–1,844, assuming that the shear-wave velocity and the frequency band for the events used in this study are 3.5 km/s and 3–15 Hz, respectively. Therefore, the anelastic attenuation in this area is low, which is in good agreement with the Precambrian stable geology of the Arabian Shield. Lower attenuation (high Q) in the Arabian Shield agrees with crustal values of Q determined by Pasyanos and others (2009). However, the value of Q estimated in this study is higher than the estimated values of 350 to 700 by Pasyanos and others (2009). This may be due to the different frequency band used in this study (3–15 Hz) as compared with Pasyanos and others (2009) (1–2 Hz). In general, it is well known that the value of Q is frequency dependent, and higher values of Q for high frequency are obtained in the continental United States (Erickson and others, 2004) and Italy (Bianco and others, 2002).

Site residuals are also derived through the regression analysis from equation 8. Since we did not take into account any site amplification factors, such as V_{S30}, site residuals are expected to correlate with site amplifications caused by near-surface geology. Positive residuals would correspond to strong site amplifications owing to soft soils, whereas the stations with negative residuals would be less amplified on hard rock sites. Figures 1.6 and 1.7 of appendix 1 compare site residuals with surface geology for PGA and PGV, respectively. Most of the sites on volcanic rocks have negative residuals, whereas all stations on sedimentary rocks have positive residuals, as previously noted. Stations on crystalline rocks can have either positive or negative residuals.

Site Residuals Compared with Estimated V_{S30}

Because of the lack of V_{S30} data, we estimated V_{S30} values for each station based on the H/V response spectral ratio using the method of Ghofrani and Atkinson (2014). Ghofrani and Atkinson (2014) evaluated the H/V response spectral ratio in comparison with V_{S30} as reported in the NGA-West2 and Japanese databases. Before calculating response spectra, we evaluated the SNR using the Fourier amplitude spectra of each record. The noise and signal parts are evaluated before the P-wave arrival and at the S-wave arrival, respectively. Our criterion is for a SNR greater than 3 (Boore and Bommer, 2005), and the highest frequency where the SNR is less than 3 is defined as the maximum frequency for each

record. We then exclude the response spectra in the frequency range less than the corresponding maximum frequency.

We calculated 5-percent-damped acceleration response spectra at 120 frequencies between 0.1 and 20 Hz using a seismograph orientation-independent measure known as RotD50 (Boore, 2010) as the horizontal component of response spectra. The obtained horizontal response spectra are then divided by the corresponding vertical response spectra to estimate H/V response spectral ratios. Finally, we take the log-average of multiple H/V spectral ratios at each station to obtain the averaged H/V response spectral ratio following the methodology of Ghofrani and Atkinson (2014):

$$\log\left(\frac{\bar{H}}{V}\right)_i = \frac{\sum_{j=1}^{N_i} \log\left(\frac{H}{V}\right)_{ij}}{N_i}, \tag{15}$$

where

N_i is the number of events recorded at station i.

Note that N_i varies for different periods and stations based on the SNR criteria described above. We then pick the peak amplitude (A_{peak}) and peak frequency (f_{peak}) of the averaged H/V response spectral ratio estimated in equation 15. The selected peak amplitude and peak frequency are used to estimate V_{S30} using the relationship derived by Ghofrani and Atkinson (2014) based on the NGA-West2 database:

$$\log(V_{S30}) = 2.80\ (\pm0.02) + 0.16\ (\pm0.02)\ \log(f_{peak}) - 0.50\ (\pm0.03)\ \log(A_{peak}), \tag{16}$$

where errors shown in this equation are 95-percent confidence intervals.

This equation is only valid for sites with peak frequencies greater than 1 Hz. We chose the relationship based on the NGA-West2 database because this database consists of global earthquakes.

A total of 75 stations are investigated using this methodology, but the averages of the H/V spectral ratios for some stations do not have clear peak amplitudes. Therefore, we selected only 15 stations to estimate their V_{S30} based on the two following criteria: (1) the station records at least three events, and (2) the station has a clear peak amplitude with low standard deviation. One successful and one unsuccessful example of averaged H/V spectral ratio are shown in figure 1.8 of appendix 1. In the successful examples, the H/V ratios have a clear single peak amplitude with low standard deviation. In contrast, the H/V ratios for the eliminated stations have unclear or multiple peak amplitudes. For the selected 15 stations, we derived V_{S30} using equation 16. The obtained values of peak amplitude, peak frequency, and V_{S30} are compared with site residuals for both PGA and PGV derived through the regression analysis in figure 13. Furthermore, we selected the 10 other stations with the flat shape of H/V spectral ratio, which indicate these stations are deployed on hard rock (Baker and others, 2021). The V_{S30} values for these 10 selected stations are assumed to be 700 m/s and are plotted as gray circles in figure 13. The derived peak amplitude and V_{S30} correlate with the site residuals, especially for PGV, whereas the derived peak frequency does not correlate with either PGA or PGV. This might be because most of the stations used in this study sit on medium- to hard-rock sites, which makes it difficult to see clear dependences as explained in Sahakian and others (2018).
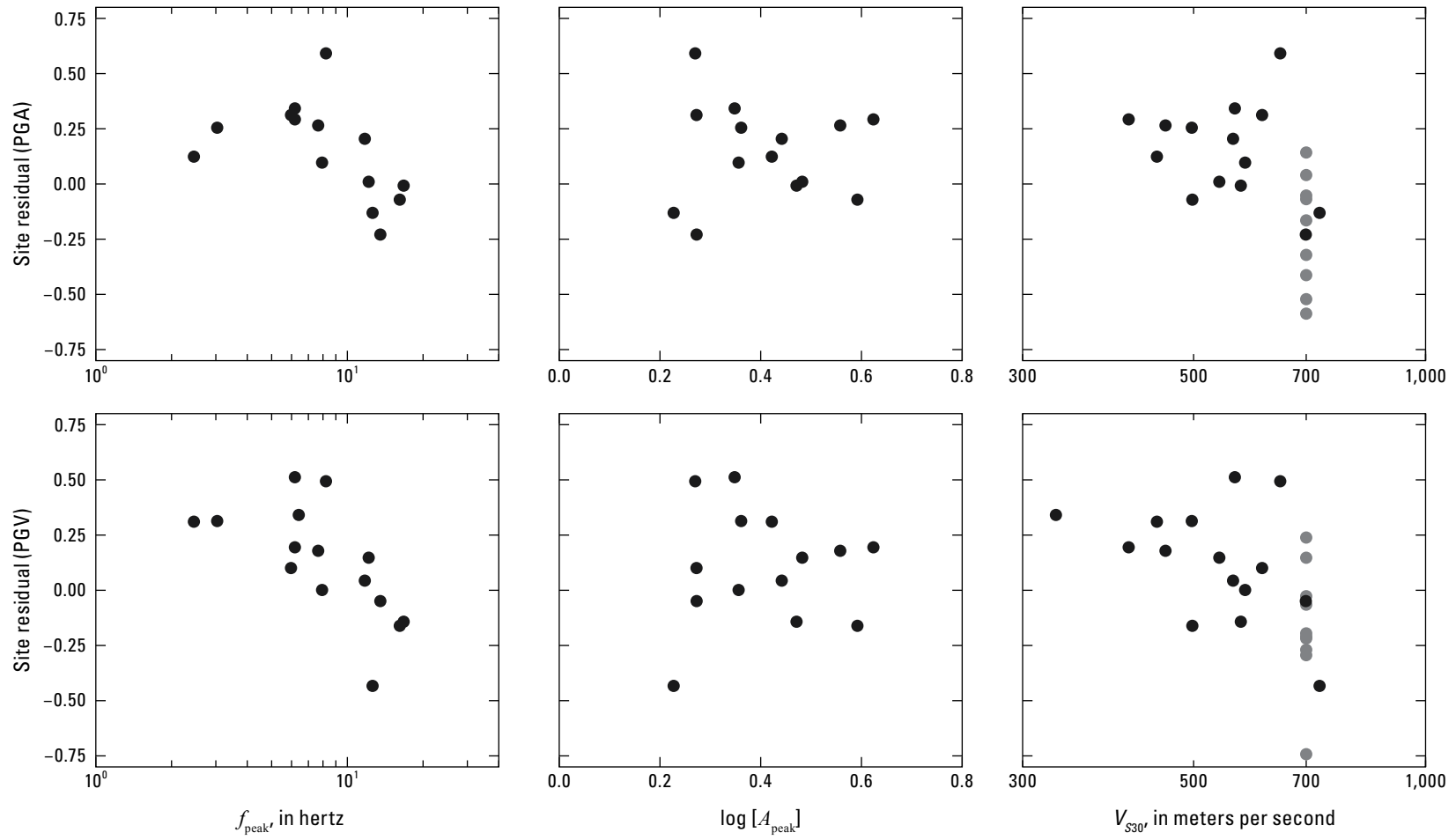
Figure 13. Plots of site residuals for peak ground acceleration (PGA) (top) and peak ground velocity (PGV) (bottom) versus peak frequency (f_{peak}), the logarithm of peak amplitude (A_{peak}), and the time averaged shear-wave velocity of the top 30 meters (V_{S30}), estimated from peak amplitude and peak frequency for each station. Gray circles are sites with flat horizontal-to-vertical spectral ratios.

Summary and Conclusions

We have created a ground-motion database for western Saudi Arabia that contains peak ground acceleration (PGA) and peak ground velocity (PGV) values for 2,770 records from 177 events. Using this dataset, we developed modified ground-motion prediction equations (GMPEs) for PGA and PGV for western Saudi Arabia based on the BSSA14 reference GMPEs (Boore and others, 2014), which were developed using a global dataset. The model presented here contains the first general GMPEs for the Kingdom of Saudi Arabia and is in good agreement with the recorded ground-motion records of western Saudi Arabia. The main modification to the reference GMPEs was the event residuals, which showed that PGAs recorded in western Saudi Arabia have smaller magnitude scaling compared to the reference GMPEs, whereas PGV data show similar scaling between the GMPEs. The estimated coefficients associated with the anelastic attenuation for PGA and PGV are smaller in absolute value compared to that of the reference GMPEs. Our Saudi Arabian GMPEs were obtained using events with magnitudes (M) between $M3$ and $M5.5$ but are extrapolated to $M7$, with the assumption of the same magnitude scaling in the range of $M > 5.5$ as in the BSSA14 model. Furthermore, the magnitude scaling of the Saudi Arabian GMPEs is made to vary smoothly, instead of using a hinge magnitude, by introducing a cubic interpolation function. On the other hand, the applicable distance range of the Saudi Arabian GMPEs is between 1 and 400 kilometers. This new western Saudi Arabian GMPE may be useful for application to seismic hazard assessments in Saudi Arabia.

Data and Resources

The seismograms used in this study were recorded by the Saudi National Seismic Network (SNSN), operated by the Saudi Geological Survey (SGS). The seismic data used may be requested from the SGS (https://sgs.gov.sa/en/e-services). Earthquake locations and moment magnitudes were determined by the SGS. These seismograms and the earthquake catalog can be requested from the SGS. The authors used open-source software Python (https://python.org/) and R (https://www.r-project.org/) to perform the analysis and create the figures. Figures 1.6 and 1.7 of appendix 1 were created using ArcGIS software (https://www.esri.com/).

Acknowledgments

References Cited

Abdelfattah, A.K., Al-Amri, A., Abd el-aal, A.K., Zaidi, F.K., Fnais, M., Almadani, S., and Al-Arifi, N., 2017, The 23 January 2014 Jizan earthquake and its tectonic implications in southwestern Saudi Arabia: Tectonophysics, v. 712–713, p. 494–502, https://doi.org/10.1016/j.tecto.2017.05.034.

Abrahamson, N., and Silva, W., 2008, Summary of the Abrahamson & Silva NGA ground-motion relations: Earthquake Spectra, v. 24, no. 1, p. 67–97, https://doi.org/10.1193/1.2924360.

Abrahamson, N.A., and Youngs, R.R., 1992, A stable algorithm for regression analyses using the random effects model: Bulletin of the Seismological Society of America, v. 82, no. 1, p. 505–510.

Aki, K., and Richards, P.G., 1980, Quantitative seismology—Theory and methods: San Francisco, Calif., W.H. Freeman and Company, 952 p.

Akkar, S., Sandıkkaya, M.A., and Bommer, J.J., 2014, Empirical ground-motion models for point- and extended-source crustal earthquake scenarios in Europe and the Middle East: Bulletin of Earthquake Engineering, v. 12, no. 1, p. 359–387, https://doi.org/10.1007/s10518-013-9461-4.

Ambraseys, N.N., Melville, C.P., and Adams, R.D., 2005, The seismicity of Egypt, Arabia, and the Red Sea—A historical review: Cambridge, United Kingdom, Cambridge University Press, 181 p.

Atkinson, G.M., 2010, Ground-motion prediction equations for Hawaii from a referenced empirical approach: Bulletin of the Seismological Society of America, v. 100, no. 2, p. 751–761, https://doi.org/10.1785/0120090098.

Atkinson, G.M., and Boore, D.M., 2006, Earthquake ground-motion prediction equations for eastern North America: Bulletin of the Seismological Society of America, v. 96, no. 6, p. 2181–2205, https://doi.org/10.1785/0120050245.

Baer, G., and Hamiel, Y., 2010, Form and growth of an embryonic continental rift—InSAR observations and modelling of the 2009 western Arabia rifting episode: Geophysical Journal International, v. 182, no. 1, p. 155–167, https://doi.org/10.1111/j.1365-246X.2010.04627.x.

Baker, J.W., Bradley B.A., and Stafford, P.J., 2021, Seismic hazard and risk analysis: Cambridge, United Kingdom, Cambridge University Press, 582 p.

Baltay, A.S., and Beroza, G.C., 2013, Ground-motion prediction from tremors: Geophysical Research Letters, v. 40, p. 6340–6345, https://doi.org/10.1002/2013GL058506.

Baltay, A.S., and Hanks, T.C., 2014, Understanding the magnitude dependence of PGA and PGV in NGA-West 2 data: Bulletin of the Seismological Society of America, v. 104, no. 6, p. 2851–2865, https://doi.org/10.1785/0120130283.

Baltay, A.S., Hanks, T.C., and Abrahamson, N.A., 2017, Uncertainty, variability, and earthquake physics in ground-motion prediction equations: Bulletin of the Seismological Society of America, v. 107, no. 4, p. 1754–1772, https://doi.org/10.1785/0120160164.

Bianco, F., Del Pezzo, E., Castellano, M., Ibanez, J., and Di Luccio, F., 2002, Separation of intrinsic and scattering seismic attenuation in the Southern Apennine zone, Italy: Geophysical Journal International, v. 150, no. 1, p. 10–22, https://doi.org/10.1046/j.1365-246X.2002.01696.x.

Bindi, D., Cotton, F., Kotha, S.R., Bosse, C., Stromeyer, D., and Grünthal, G., 2017, Application-driven ground motion prediction equation for seismic hazard assessments in non-cratonic moderate-seismicity areas: Journal of Seismology, v. 21, no. 5, p. 1201–1218, https://doi.org/10.1007/s10950-017-9661-5.

Bird, P., 2003, An updated digital model of plate boundaries: Geochemistry Geophysics Geosystems, v. 4, no. 3, https://doi.org/10.1029/2001GC000252.

Boore, D.M., 1983, Stochastic simulation of high-frequency ground motions based on seismological models of the radiated spectra: Bulletin of the Seismological Society of America, v. 73, p. 1865–1894.

Boore, D.M., 2010, Orientation-independent, nongeometric-mean measures of seismic intensity from two horizontal components of motion: Bulletin of the Seismological Society of America, v. 100, no. 4, p. 1830–1835, https://doi.org/10.1785/0120090400.

Boore, D. M., and Bommer, J.J., 2005, Processing of strong motion accelerograms—Needs, options and consequences: Soil Dynamics and Earthquake Engineering, v. 25, p. 93–115, https://doi.org/10.1016/j.soildyn.2004.10.007.

Boore, D.M., Stewart, J.P., Seyhan, E., and Atkinson, G.M., 2014, NGA-West2 equations for predicting PGA, PGV, and 5% damped PSA for shallow crustal earthquakes: Earthquake Spectra, v. 30, no. 3, p. 1057–1085, https://doi.org/10.1193/070113EQS184M.

Borcherdt, R.D., 2002, Empirical evidence for site coefficients in building code provisions: Earthquake Spectra, v. 18, no. 2, p. 189–217, https://doi.org/10.1193/1.1486243.

Bozorgnia, Y., Abrahamson, N.A., Al Atik, L., Ancheta, T.D., Atkinson, G.M., Baker, J.W., Baltay, A., Boore, D.M., Campbell, K.W., Chiou, B.S.-J., Darragh, R., Day, S., Donahue, J., Graves, R.W., Gregor, N., Hanks, T., Idriss, I.M., Kamai, R., Kishida, T., Kottke, A., Mahin, S.A., Rezaeian, S., Rowshandel, B., Seyhan, E., Shahi, S., Shantz, T., Silva, W., Spudich, P., Stewart, J.P., Watson-Lamprey, J., Wooddell, K., and Youngs, R., 2014, NGA-West2 Research Project: Earthquake Spectra, v. 30, no. 3, p. 973–987, https://doi.org/10.1193/072113EQS209M.

Bradley, B.A., 2013, A New Zealand-specific pseudospectral acceleration ground-motion prediction equation for active shallow crustal earthquakes based on foreign models: Bulletin of the Seismological Society of America, v. 103, no. 3, p. 1801–1822, https://doi.org/10.1785/0120120021.

Brune, J., 1970, Tectonic stress and the spectra of seismic shear waves from earthquakes: Journal of Geophysical Research, v. 75, p. 4997–5009.

Chiou, B.-J., and Youngs, R.R., 2008, An NGA model for the average horizontal component of peak ground motion and response spectra: Earthquake Spectra, v. 24, no. 1, p. 173–215, https://doi.org/10.1193/1.2894832.

Dobry, R., Borcherdt, R.D., Crouse, C.B., Idriss, I.M., Joyner, W.B., Martin, G.R., Power, M.S., Rinne, E.E., and Seed, R.B., 2000, New site coefficients and site classification system used in recent building seismic code provisions: Earthquake Spectra, v. 16, no. 1, p. 41–67, https://doi.org/10.1193/1.1586082.

Eissler, H.K., and Kanamori, H., 1987, A single-force model for the 1975 Kalapana, Hawaii, earthquake: Journal of Geophysical Research, v. 92, no. B6, p. 4827–4836, https://doi.org/10.1029/JB092iB06p04827.

El-Isa, Z.H., and Al Shanti, A., 1989, Seismicity and tectonics of the Red Sea and western Arabia: Geophysical Journal International, v. 97, no. 3, p. 449–457, https://doi.org/10.1111/j.1365-246X.1989.tb00515.x.

Erickson, D., McNamara, D.E., and Benz, H.M., 2004, Frequency-dependent Lg Q within the continental United States: Bulletin of the Seismological Society of America, v. 94, no. 5, p. 1630–1643, https://doi.org/10.1785/012003218.

Ghofrani, H., and Atkinson, G.M., 2014, Site condition evaluation using horizontal-to-vertical response spectral ratios of earthquakes in the NGA-West 2 and Japanese databases: Soil Dynamics and Earthquake Engineering, v. 67, p. 30–43, https://doi.org/10.1016/j.soildyn.2014.08.015.

Gülerce, Z., Kargoiğlu, B., and Abrahamson, N.A., 2016, Turkey-adjusted NGA-W1 horizontal ground motion prediction models: Earthquake Spectra, v. 32, no. 1, p. 75–100, https://doi.org/10.1193/022714EQS034M.

Gupta, A., Baker, J.W., and Ellsworth, W.L., 2017, Assessing ground-motion amplitudes and attenuation for small-to-moderate induced and tectonic earthquakes in the Central and Eastern United States: Seismological Research Letters, v. 88, no. 5, p. 1379–1389, https://doi.org/10.1785/0220160199.

Hanks, T.C., and McGuire, R.K., 1981, The character of high-frequency strong ground motion: Bulletin of the Seismological Society of America, v. 71, p. 2071–2095.

Hansen, S.E., DeShon, H.R., Moore-Driskell, M.M., and Al-Amri, A.M.S., 2013, Investigating the P wave velocity structure beneath Harrat Lunayyir, northwestern Saudi Arabia, using double-difference tomography and earthquakes from the 2009 seismic swarm: Journal of Geophysical Research—Solid Earth, v. 118, no. 9, p. 4814–4826, https://doi.org/10.1002/jgrb.50286.

Hofstetter, A., Dorbath, C., and Dorbath, L., 2014, Instrumental data on the seismic activity along the Dead Sea Transform, *in* Garfunkel, Z., Ben-Avraham, Z., and Kagan, E., eds., Dead Sea transform fault system—Review: Netherlands, Springer, Dordrecht, Modern Approaches to Solid Earth Sciences, v. 6, 16 p.

Jónsson, S., 2012, Tensile rock mass strength estimated using InSAR: Geophysical Research Letters, v. 39, no. 21, article L21305, 5 p., https://doi.org/10.1029/2012GL053309.

Kehoe, H.L., Kiser, E.D., and Okubo, P.G., 2019, The rupture process of the 2018 M_w 6.9 Hawai‘i earthquake as imaged by a genetic algorithm-based back-projection technique: Geophysical Research Letters, v. 46, no. 5, p. 2467–2474, https://doi.org/10.1029/2018GL080397.

Munafò, I., Malagnini, L., and Chiaraluce, L., 2016, On the relationship between M_w and M_L for small earthquakes: Bulletin of the Seismological Society of America, v. 106, no. 5, p. 2402–2408, https://doi.org/10.1785/0120160130.

Nehlig, P., Genna, A., and Asirfane, F., 2002, A review of the Pan-African evolution of the Arabian Shield: GeoArabia, v. 7, p. 103–124.

Pallister, J.S., McCausland, W.A., Jónsson, S., Lu, Z., Zahran, H.M., El Hadidy, S., Aburukbah, A., Stewart, I.C.F., Lundgren, P.R., White, R.A., and Moufti, M.R.H., 2010, Broad accommodation of rift-related extension recorded by dyke intrusion in Saudi Arabia: Nature Geoscience, v. 3, no. 10, p. 705–712, https://doi.org/10.1038/ngeo966.

Pankow, K.L., and Pechmann, J.C., 2004, The SEA99 ground-motion predictive relations for extensional tectonic regimes—Revisions and a new peak ground velocity relation: Bulletin of the Seismological Society of America, v. 94, no. 1, p. 341–348, https://doi.org/10.1785/0120050184.

Pasyanos, M.E., Walter, W.R., and Matzel, E.M., 2009, A simultaneous multiphase approach to determine P-wave and S-wave attenuation of the crust and upper mantle: Bulletin of the Seismological Society of America, v. 99, no. 6, p. 3314–3325, https://doi.org/10.1785/0120090061.

Power, M., Chiou, B., Abrahamson, N., Bozorgnia, Y., Shantz, T., and Roblee, C., 2008, An overview of the NGA project: Earthquake Spectra, v. 24, no. 1, p. 3–21, https://doi.org/10.1193/1.2894833.

Sahakian, V., Baltay, A., Hanks, T., Buehler, J., Vernon, F., Kilb, D., and Abrahamson, N., 2018, Decomposing leftovers—Event, path, and site residuals for a small-magnitude Anza region GMPE: Bulletin of the Seismological Society of America, v. 108, p. 2478–2492, http://doi:10.1785/0120170376.

Scasserra, G., Stewart, J.P., Bazzurro, P., Lanzo, G., and Mollaioli, F., 2009, A comparison of NGA ground-motion prediction equations to Italian data: Bulletin of the Seismological Society of America, v. 99, no. 5, p. 2961–2978, https://doi.org/10.1785/0120080133.

Seyhan, E., and Stewart, J.P., 2014, Semi-empirical nonlinear site amplification from NGA-West2 data and simulations: Earthquake Spectra, v. 30, no. 3, p. 1241–1256, https://doi.org/10.1193/063013EQS181M.

Shoja-Taheri, J., Naserieh, S., and Hadi, G., 2010, A test of the applicability of NGA models to the strong ground-motion data in the Iranian plateau: Journal of Earthquake Engineering, v. 14, no. 2, p. 278–292, https://doi.org/10.1080/13632460903086051.

Spudich, P., Joyner, W.B., Lindh, A.G., Boore, D.M., Margaris, B.M., and Fletcher, J.B., 1999, SEA99—A revised ground motion prediction relation for use in extensional tectonic regimes: Bulletin of the Seismological Society of America, v. 89, p. 1156–1170.

Youssef, S.E.-H., 2015, Seismicity and seismotectonic setting of the Red Sea and adjacent areas, *in* Rasul, M.A., and Stewart, I.C.F., eds., The Red Sea—The formation, morphology, oceanography, and environment of a young ocean basin: Berlin/Heidelberg, Springer Earth Systems Science, Springer, p. 151–159.

Zahran, H.M., Sokolov, V., Roobol, M.J., Stewart, I.C.F., Youssef, S.E.-H., and El-Hadidy, M., 2016, On the development of a seismic source zonation model for seismic hazard assessment in western Saudi Arabia: Journal of Seismology, v. 20, no. 3, p. 747–769, https://doi.org/10.1007/s10950-016-9555-y.

Zahran, H.M., Sokolov, V., Youssef, S.E.-H., and Alraddadi, W.W., 2015, Preliminary probabilistic seismic hazard assessment for the Kingdom of Saudi Arabia based on combined areal source model—Monte Carlo approach and sensitivity analyses: Soil Dynamics and Earthquake Engineering, v. 77, p. 453–468, https://doi.org/10.1016/j.soildyn.2015.06.011.

Zhao, J.X., Zhang, J., Asano, A., Ohno, Y., Oouchi, T., Takahashi, T., Ogawa, H., Irikura, K., Thio, H.K., Somerville, P.G., Fukushima, Y., and Fukushima, Y., 2006, Attenuation relations of strong ground motion in Japan using site classification based on predominant period: Bulletin of the Seismological Society of America, v. 96, no. 3, p. 898–913, https://doi.org/10.1785/0120050122.

Appendix 1.   Supplemental Figures

This appendix includes eight figures. The four records of high-pass filtered displacement and velocity waveforms are plotted in figure 1.1. Distribution of the event residuals from the reference and modified ground-motion prediction equations (GMPEs) with respect to event depths is shown in figure 1.2. Figures 1.3 and 1.4 show the comparison between the Saudi Arabian GMPEs and observed data for unknown and strike-slip fault events. Figure 1.5 shows the Fourier spectra for all long-distance records (Joyner-Boore distance [R_{JB}] $\geq$200 kilometers) for acceleration waveforms to examine the dominant frequencies used to calculate the seismic quality factor Q of anelastic attenuation. Figures 1.6 and 1.7 compare station residuals obtained through regression analysis with surface geology for peak ground acceleration (PGA) and peak ground velocity (PGV). Figure 1.8 shows an example of the horizontal-to-vertical (H/V) response spectral ratio estimated at stations QLBS and TBKS.
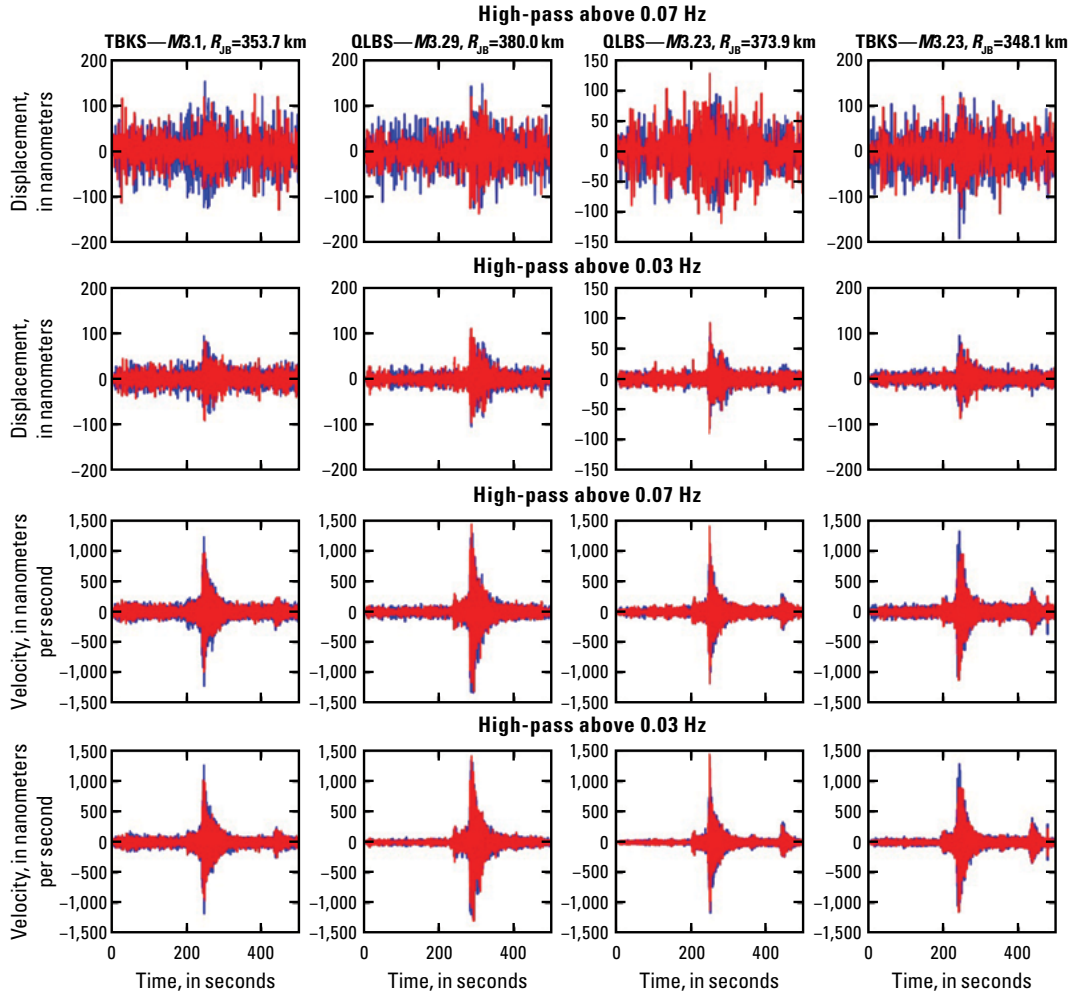
Figure 1.1.   Plots of displacement (rows 1 and 2) and velocity (rows 3 and 4) versus time showing four examples of high-pass filtered displacement and velocity waveforms with cutoff frequencies (0.07 and 0.3 hertz [Hz]) for long-distance records of small events at stations TBKS and QLBS. Red and blue lines display the east-west and north-south components, respectively. M, magnitude; R_{JB}, Joyner-Boore distance; km, kilometer.
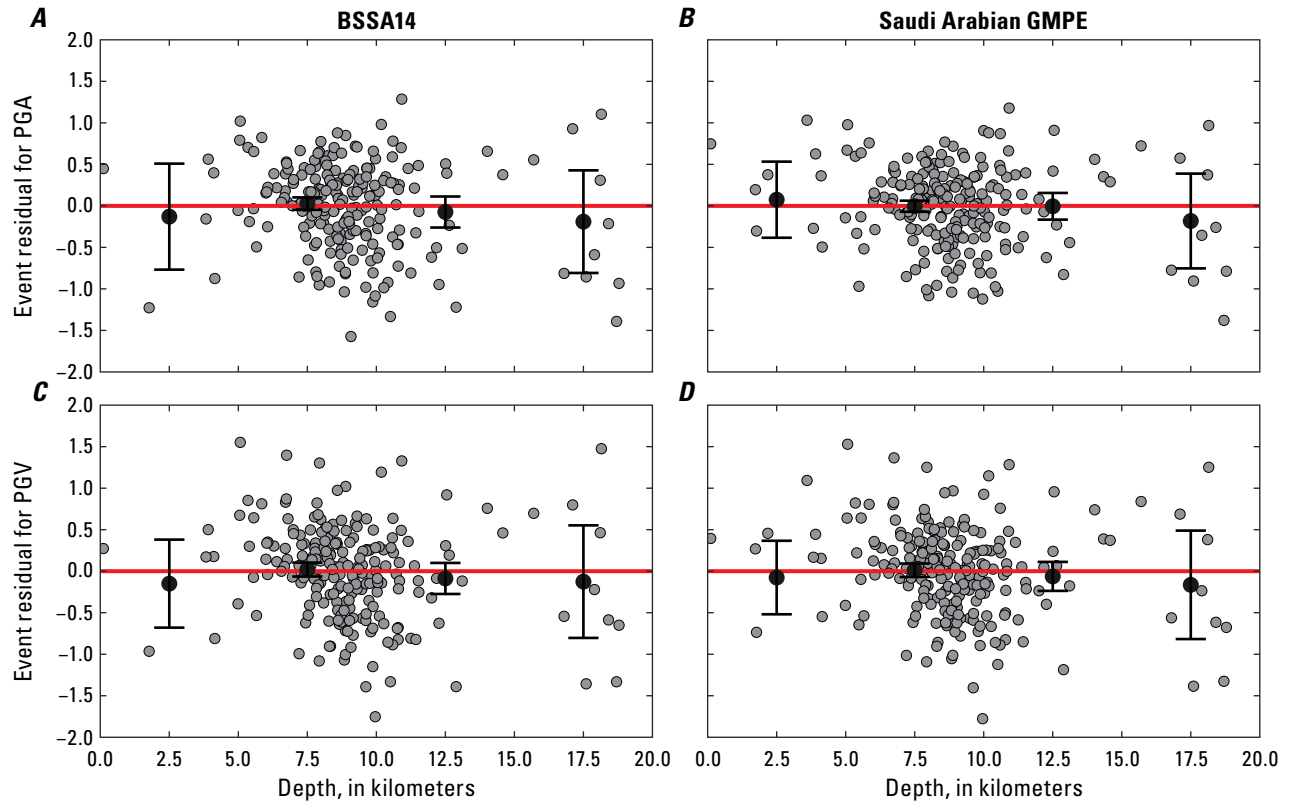
Figure 1.2.   Plots of event residuals for peak ground acceleration (PGA) (top) and peak ground velocity (PGV) (bottom) versus event depth. *A* and *C*, Event residuals from the BSSA14 model. *B* and *D*, Event residuals from the Saudi Arabian ground-motion prediction equations (GMPEs).
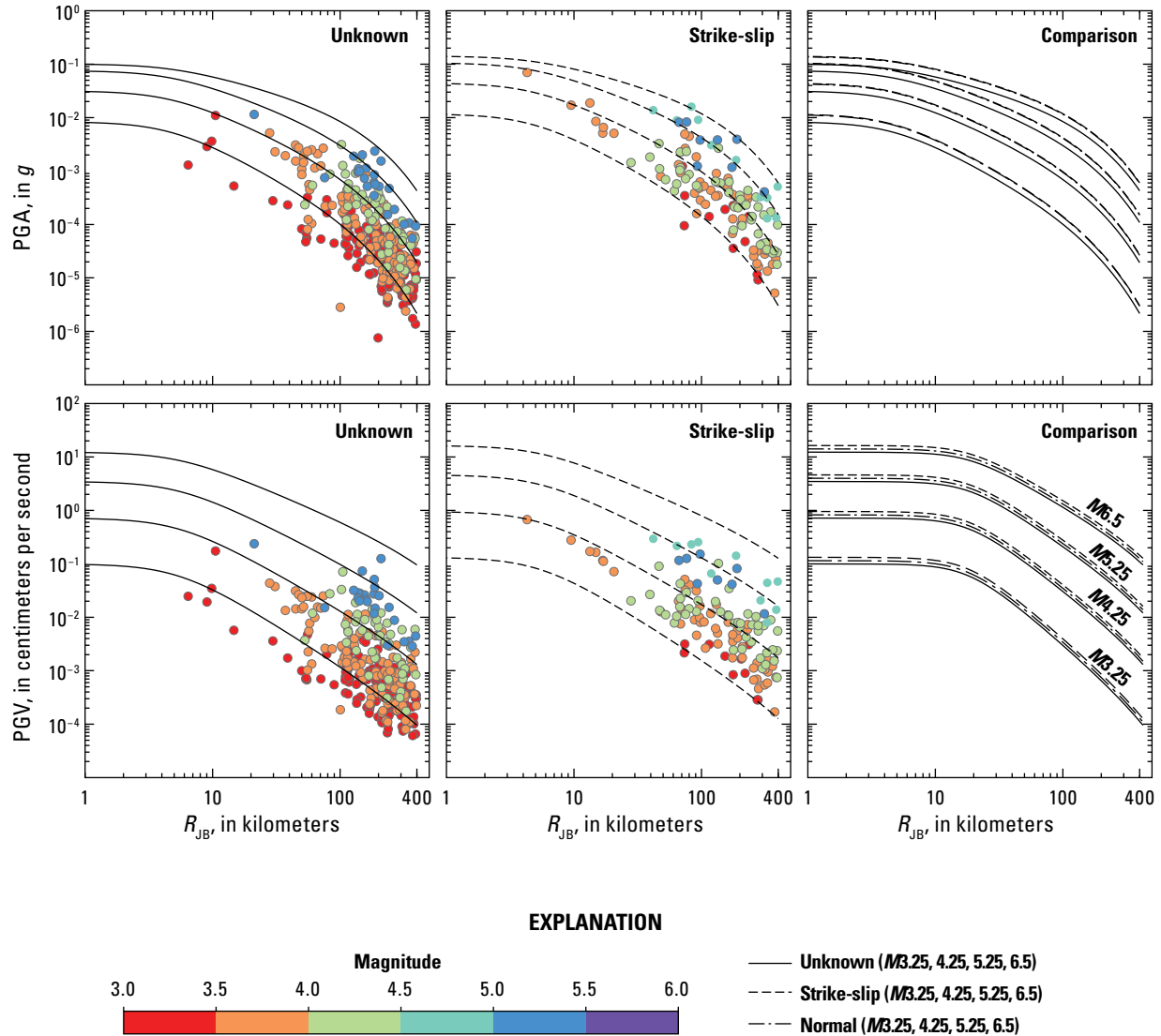
Figure 1.3. Plots of peak ground acceleration (PGA) (top) and peak ground velocity (PGV) (bottom) versus Joyner-Boore distance (R_{JB}) comparing events from the Saudi Arabian ground-motion prediction equations (GMPEs) (black lines) with observed data (color of dots corresponds to magnitude [M]). Left, Events with unknown fault mechanisms. Center, Events with strike-slip fault mechanisms. Right, A comparison of the Saudi Arabian GMPEs using different focal mechanisms (unknown, strike-slip, and normal faulting) for M3.25, M4.25, M5.25, and M6.5 earthquakes. g, acceleration due to gravity.
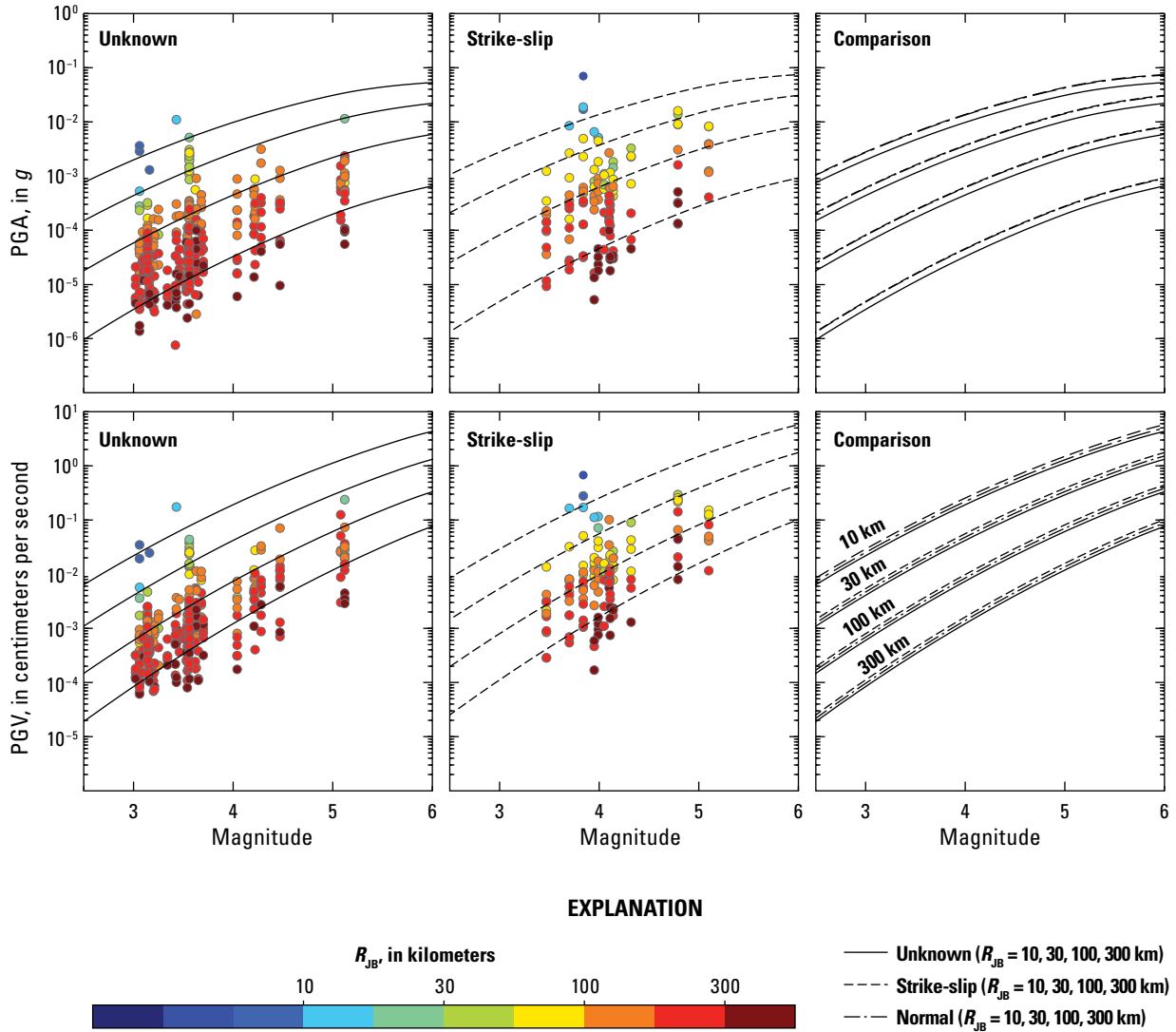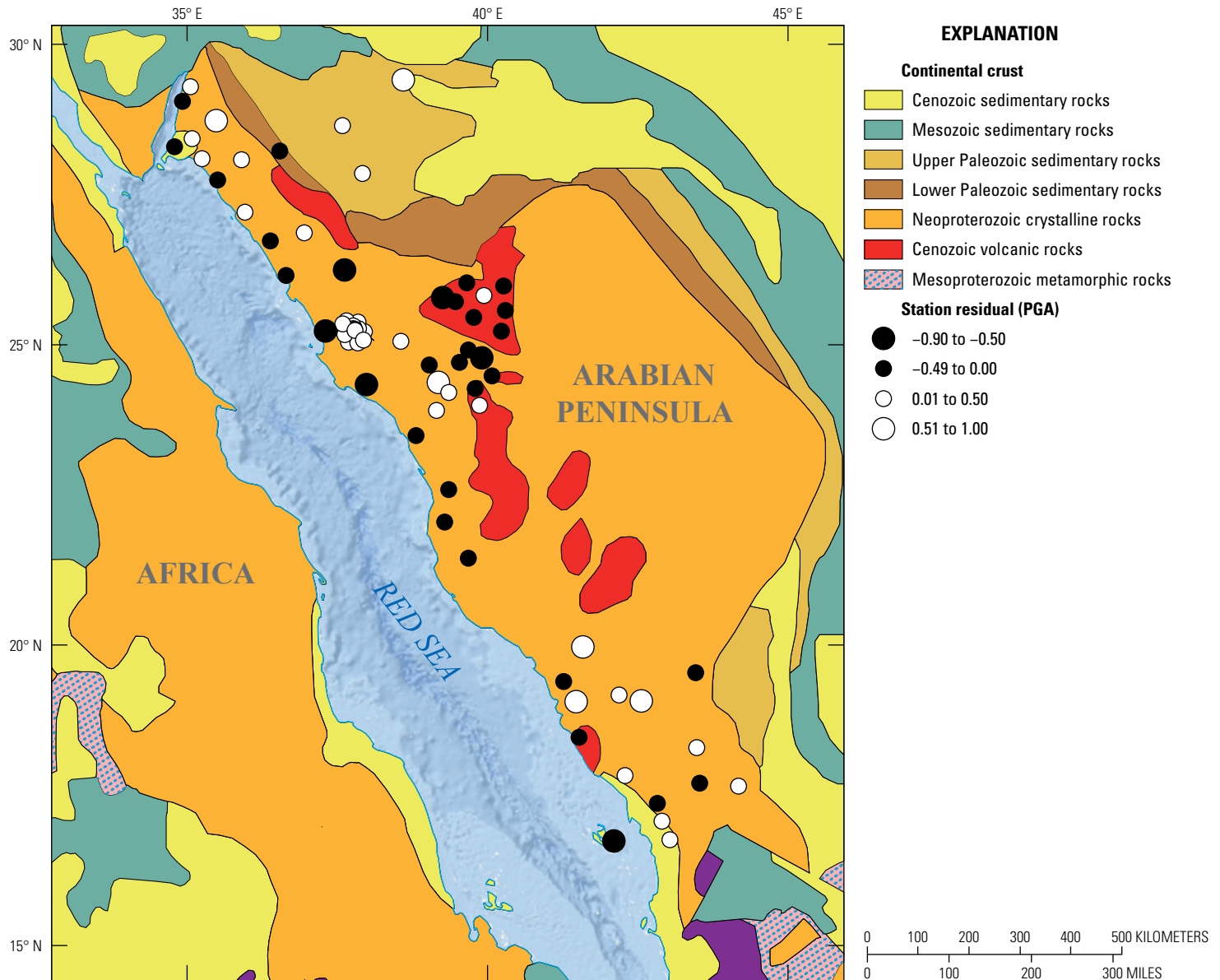
Figure 1.4. Plots of peak ground acceleration (PGA) (top) and peak ground velocity (PGV) (bottom) versus magnitude comparing the Saudi Arabian ground-motion prediction equations (GMPEs) (black lines) with observed data (color of dots corresponds to magnitude). Left, Events with unknown fault mechanisms. Center, Events with strike-slip fault mechanisms. Right, A comparison of the Arabian GMPEs using different focal mechanisms (unknown, strike-slip, and normal faulting) for Joyner-Boore distances (R_{JB}) of 10, 30, 100, and 300 kilometers (km). g, acceleration due to gravity.
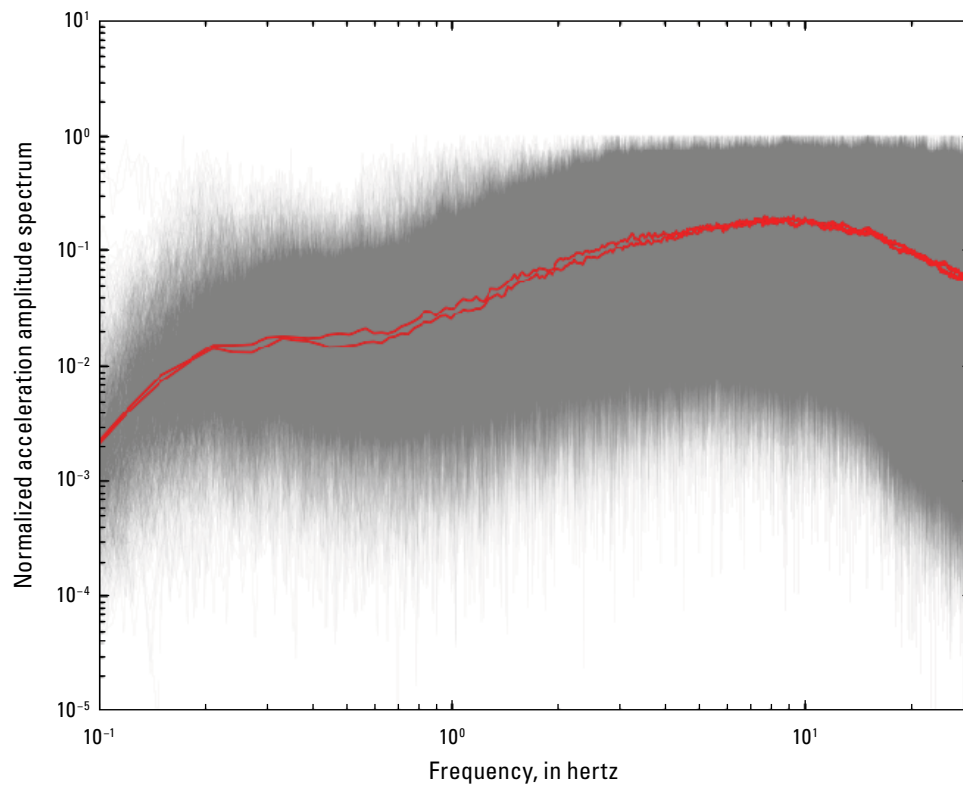
Figure 1.5.   Plot of Fourier spectra for all long-distance records (Joyner-Boore distances [R_{JB}] ≥200 kilometers) for acceleration waveforms. Gray lines show individual spectral peaks and red lines are the geometrical mean for two different horizontal components.

Figure 1.6.   Geologic map of western Saudi Arabia (Nehlig and others, 2002) showing station residuals for peak ground acceleration (PGA). White circles are positive residuals and black circles are negative residuals. Size of circle corresponds to strength of ground-motion amplification at a site.
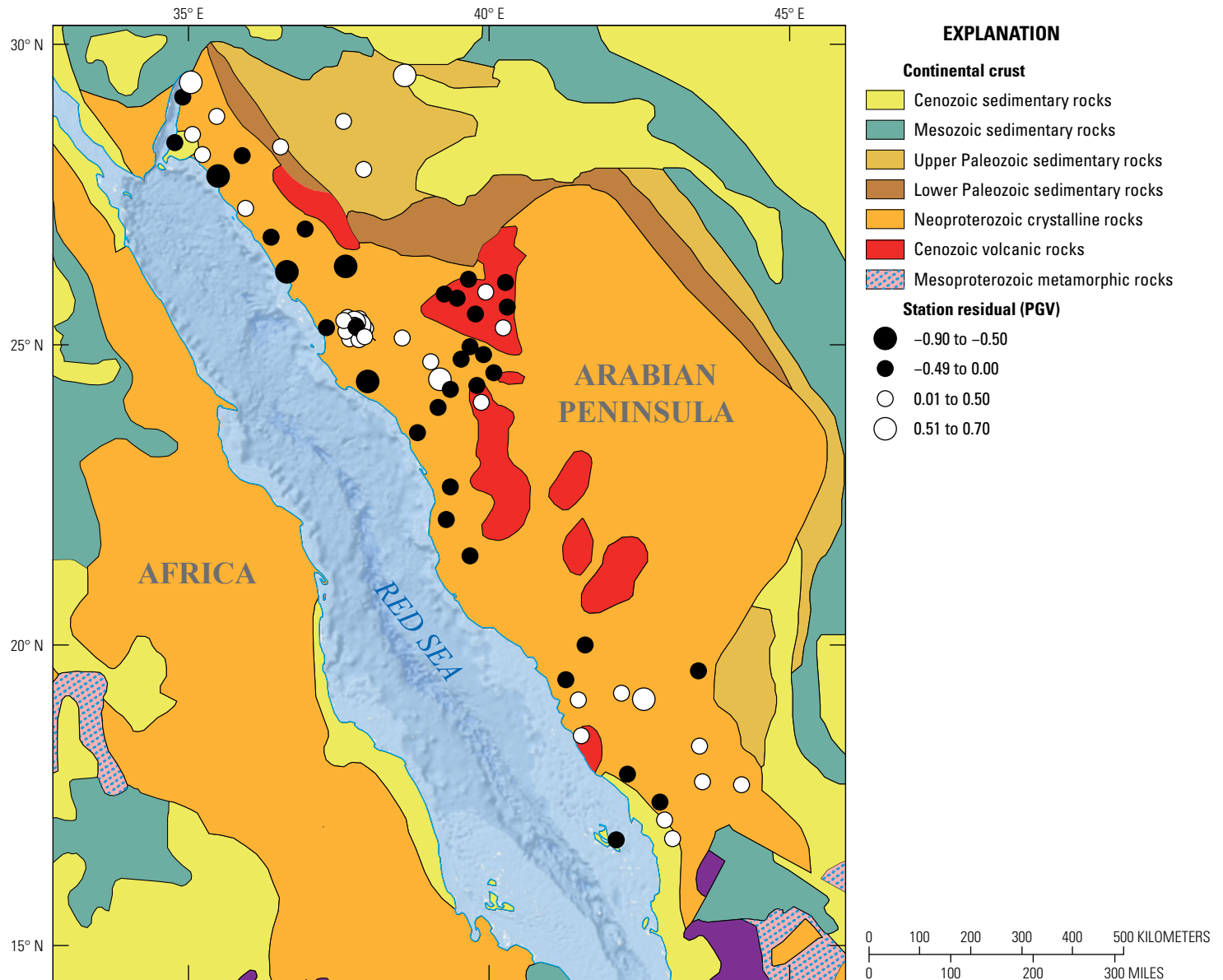
Figure 1.7.   Geologic map of western Saudi Arabia (Nehlig and others, 2002) showing station residuals for peak ground velocity (PGV). White circles are positive residuals and black circles are negative residuals. Size of circle corresponds to strength of ground-motion amplification at a site.
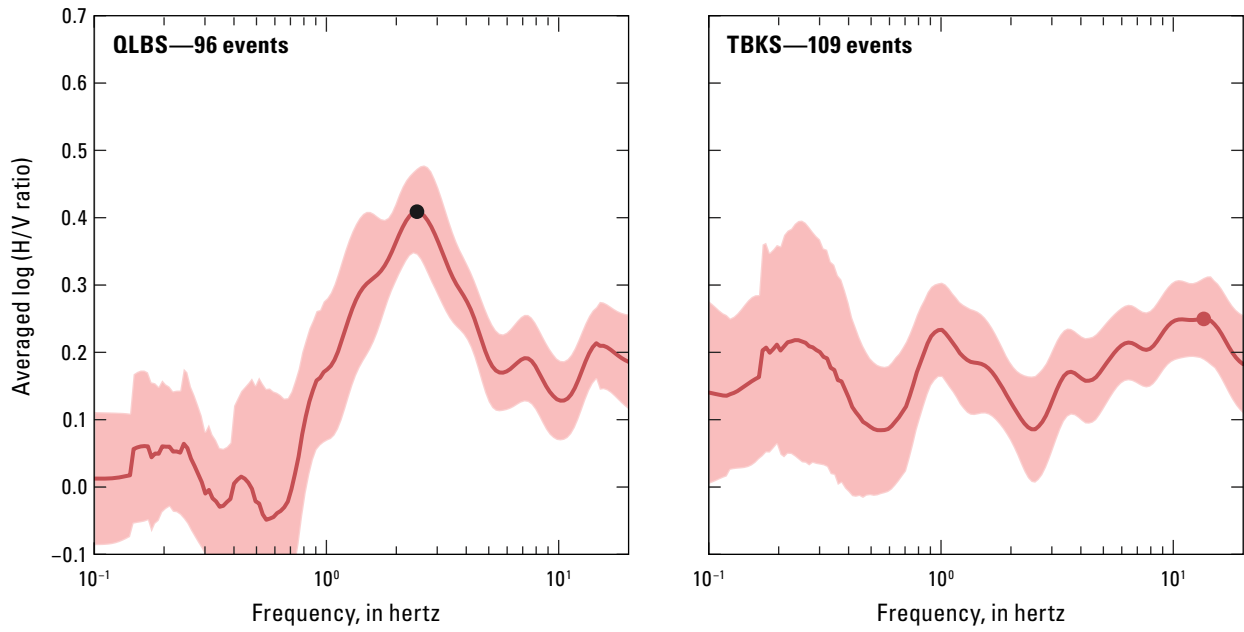
Figure 1.8.   Plots showing examples of estimated mean horizontal-to-vertical response spectral ratio (H/V ratio) at stations QLBS (left) and TBKS (right). Red shaded area is the 1-standard-deviation band of spectral ratios. For station QLBS, the mean H/V response spectral ratio shows a clear single peak (black dot) at 2.5 hertz, whereas station TBKS has multiple minor peaks with a maximum peak (red dot) at 15 hertz.